

AD-A162 726

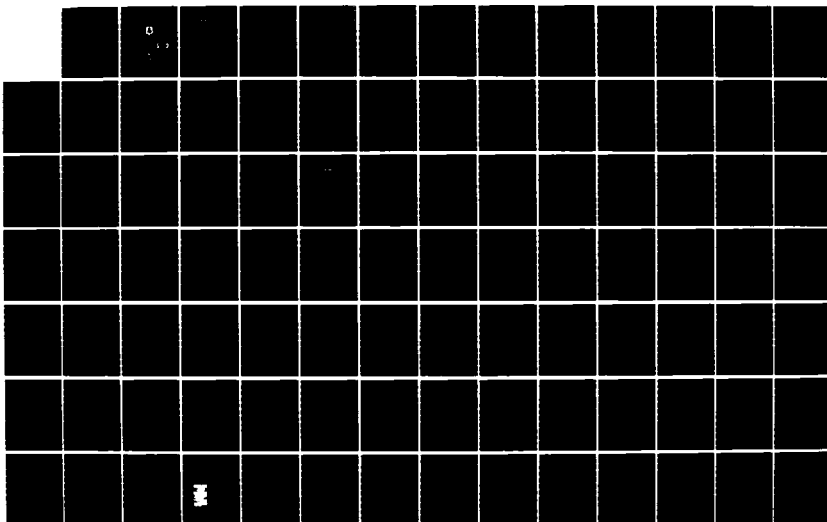
ACTA MECHANICA SINICA (SELECTED ARTICLES) (U) FOREIGN
TECHNOLOGY DIV WRIGHT-PATTERSON AFB OH X YIN ET AL.
05 DEC 85 FTD-ID(RS)T-0494-85

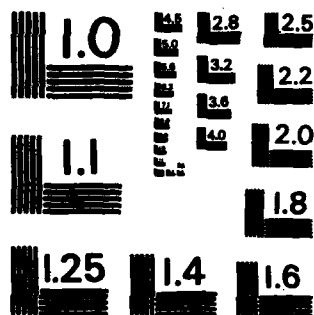
1/2

UNCLASSIFIED

F/G 20/4

NL





MICROCOPY RESOLUTION TEST CHART
NATIONAL BUREAU OF STANDARDS-1963-A

2

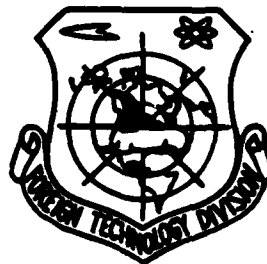
FTD-ID(RS)T-0494-85

FOREIGN TECHNOLOGY DIVISION



ACTA MECHANICA SINICA
(SELECTED ARTICLES)

DTIC
ELECTE
S DEC 30 1985 D
D



AD-A162 726

DTIC FILE COPY

Approved for public release;
distribution unlimited.

85 12 30 090

EDITED TRANSLATION

FTD-ID(RS)T-0494-85

5 Dec 85

MICROFICHE NR: FTD-85-C-001208

ACTA MECHANICA SINICA (SELECTED ARTICLES)

English pages: 121

Source: Lixue Xuebao, Nr. 5, 1984, pp. 454-475; 485-520

Country of origin: China

Translated by: SCITRAN

F33657-84-D-0165

Requester: FTD/TQTA

Approved for public release; distribution unlimited.

THIS TRANSLATION IS A RENDITION OF THE ORIGINAL FOREIGN TEXT WITHOUT ANY ANALYTICAL OR EDITORIAL COMMENT. STATEMENTS OR THEORIES ADVOCATED OR IMPLIED ARE THOSE OF THE SOURCE AND DO NOT NECESSARILY REFLECT THE POSITION OR OPINION OF THE FOREIGN TECHNOLOGY DIVISION.

PREPARED BY:

TRANSLATION DIVISION
FOREIGN TECHNOLOGY DIVISION
WP-AFB, OHIO.

Table of Contents:

Graphics Disclaimer	ii
Investigation of Rolling-up and Interaction of Leading-edge and Trailing-edge Vortex Sheets on a Slender Delta Wing; by Yin Xieyuan, Xia Nan, Deng Guohua	1
Calculation of Circular Jet with Particles Impacting Upon a Plate; By Liu Dayou	21
A Non-local Elastic Plastic Continuum Model and the Distress Distribution Near a Cracked Tip; by Yu Jilin, Zheng Zhemin	46
Study of Plane Stress with Elastic Plastic Mixed Mode Fracture; by Xu Jilin, Xue Yinian, Han Jinghu	70
An Analytical Solution of Dynamic Response for Ideal Rigid Plastic Timoshenko Beam, by Jin Quanlin	90
General Variational Theorem for Structural Plastic Buckling Analysis Using Deformation Theory, by Li Guochen	106

Accession For	
NTIS CR&I	<input checked="" type="checkbox"/>
DTIC TAB	<input type="checkbox"/>
Unannounced	<input type="checkbox"/>
Justification	
By	
Distribution	
Availability Codes	
Dist	Avail and/or Special
A-1	



GRAPHICS DISCLAIMER

All figures, graphics, tables, equations, etc. merged into this translation were extracted from the best quality copy available

Investigation of Rolling-up and Interaction of Leading-edge and Trailing-edge Vortex Sheets on a Slender Delta Wing

Yin Xieyuan, Xia Nan and Deng Guohua

(University of Science and Technology of China)

Abstract

The objective of this paper is to establish a simple two-dimensional theoretical model in an attempt to use a computer to numerically simulate the experimental results of Hummel regarding the rolling-up and interaction of the leading-edge and trailing-edge vortex sheets on a delta wing. It was found experimentally that when the leading vortex is present the trailing-edge vortex sheet will roll up another vortex downstream from the trailing-edge. Furthermore, the circulation of the leading-edge vortex is opposite in direction to that of the trailing-edge vortex. The numerical results are in good agreement with the experimental pictures.

I. Introduction

One of the problems of major concern for researchers in aerodynamics and aircraft designers is the non-linear aerodynamic characteristics caused by the separation of body and wing vortices of the aircraft at large angles of attack. Effective utilization of the additional lift generated by body and wing vortices can improve the aerodynamic properties of the aircraft and increase the maneuverability. To study the mechanism of formation of body and wing vortices and the complicated

interaction between various vortex systems as well as between vortices and the aircraft in detail is the key to the accurate estimation of various non-linear force and torque terms on the aircraft. Therefore, the study of vortex motion has important practical values.

The study of the leading-edge vortex of a slender delta wing began in the forties and fifties. There are significant advances in recent years. In addition to measuring force and pressure, recent experimental studies focused on the application of display technique to the flow field as well as on the detection of fine details of the spatial flow field. Based on the "contours" of total pressure, static pressure and dynamic pressure measured, as well as on the spatial distribution of the flow direction, we can have a more direct and profound understanding of the vortex flow field.

In the early stage, the theoretical study of leading-edge vortex was based on the conic flow assumption which simplified a three-dimensional flow problem to a two-dimensional problem on a transverse plane, including the work done by C.E. Brown and W.H. Michael^[1], K.W. Mangler and J.H.B. Smith^[2], and the later improvement made by J.H.B. Smith^[3]. The Smith model divides the vortex layer into two points. The outer part uses a broken line section to replace the vortex layer. The inner part uses a concentrated vortex to represent the core and a "vortex transport line" to connect inner and outer regions. The model could be used to obtain the shape of the vortex layer, and the strength and intensity of the core. However, the accuracy is not

desirable. After computers are extensively used, a vortex lattice method with leading-edge separation vortex, introduced by C.M. BesouepkoBckHH^[5] and O.A. Kandil, D.T. Mook and A.H. Nayfeh^[6], is a representative method. The leading-edge vortex layer is replaced by several discrete vortex threads. Through iterations, the position of free vortex threads are determined. The boundary conditions on the wing surface are also simultaneously satisfied. In order to accurately calculate the load distribution on the wing, P.E. Rubbert et al^[7] introduced the "free vortex layer" method by using higher order surface elements. It can be used to calculate the shape of non-conical flow fields and vortex layers, as well as the load distribution on the entire wing.

All the experimental and theoretical studies discussed above are focused on the rolling-up of the leading-edge vortex layer, the force and torque characteristics, and the calculation of load distribution. It seems that there is little work done on the development of leading-edge vortex at downstream from the trailing-edge and the interaction between leading-edge and trailing-edge vortices. We are very much

Manuscript received on April 27, 1983.

intrigued by the work done by D. Hummel^[8]. Hummel performed a /455 series of fine manuscripts. In particular, he did an experimental study of the interaction between leading-edge and trailing-edge vortices. From his measured total pressure, static pressure and spatial flow direction distribution, we can see that

two spiral vortices are gradually formed downstream from the trailing-edge. One is the leading-edge vortex and the other is the vortex rolled-up by the trailing vortex layer. The circulations of these two vortices are opposite in direction. A schematic diagram of the flow pattern is shown in Figure 1.

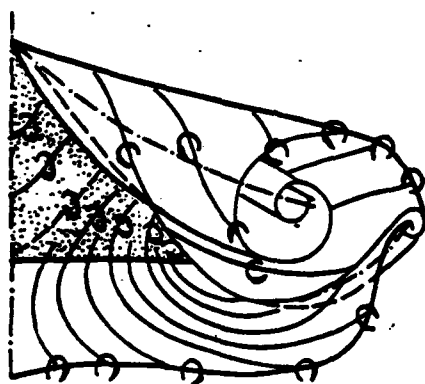


Figure 1. Schematic Diagram for the Formation of Downstream Vortices of a Slender Delta Wing

Inspired by Hummel's experiment results, we attempted to establish a simple theoretical model to simulate Hummel's results numerically on a computer. This study will benefit the understanding of the structure of a down wash flow field.

II. Theoretical Analysis

In order to study the interaction between leading-edge and trailing-edge vortices, we must first obtain the shape, position and strength of the rolling-up of the leading-edge at the trailing-edge. In addition, we must also have the intensity distribution of the trailing-edge vortex, i.e., the vortex

intensity, or spanwise circulation, distribution on the wing. Figures 2 and 3 show the pressure distribution on the wing surface and the vortex line shape measured by Hummel. From the figures, one can see that the surface pressure distribution and the vortex line are essentially different from those obtained based on the linearized slender wing theory of Jones due to the presence of the leading-edge vortex. However, as compared to Smith's^[3] theory, the shape of the pressure distribution, the position of the suction peak and the shape of the vortex are qualitatively similar. However, there are some differences quantitatively. In other words, as a preliminary theoretical investigation, a two-dimensional model can reflect the major characteristics of the flow field. But, we did not choose Smith's vortex layer model. Instead, a simpler two-dimensional unsteady flow analogy was used. Our theoretical model was built based on a discrete vortex method, which does not require iterations to solve a set of non-linear equations.

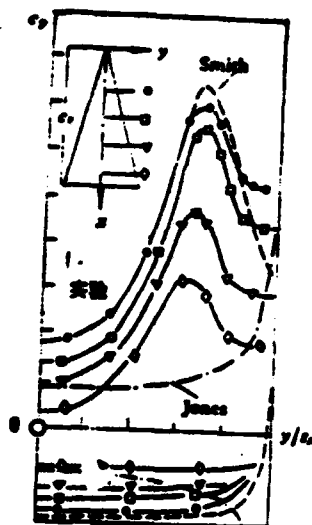


Figure 2. Pressure distribution on Delta wing $A=1$
 $\alpha=20.5$
 1--experimental

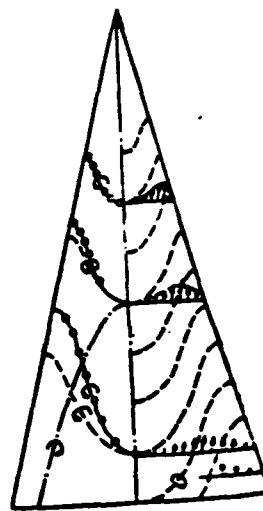


Figure 3. Adhered vortex vector (right) and adhered vortex line (left)

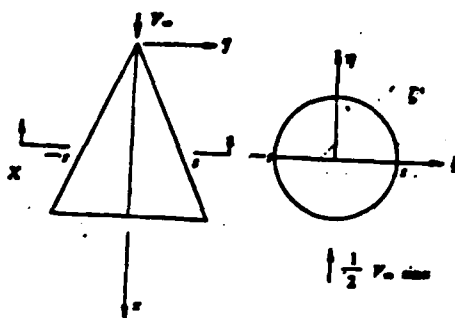


图 4 二维理论模型示意图

Figure 4. Coordinate systems definition

It is an initial value problem of a series of normal differential equations. It is not limited to the "conic flow" assumption which will facilitate the extension to more complicated airfoils. It also facilitates the further consideration of "secondary vortex" separation problems. /456

Based on the two-dimensional unsteady flow analogy, the three-dimensional flow of a delta wing with an attack angle can be considered as an unsteady flow around a two-dimensional plate in the x plane. The width of the plate at any time corresponds to the wing span in the x position. When the flow passes the edge of the plate, the boundary layer is separated. A free shear layer is formed due to the velocity difference between the upper and lower surface. Based on existing studies, it is known that, as long as it does not involve the mechanism of separation (which is a viscosity effect), the free shear layer after separation can be assumed as an inviscid vortex layer. As a next step, the vortex layer is replaced by several discrete point vortices. Therefore, the flow around the plate satisfies Laplace equation

$$\frac{\partial^2 \varphi}{\partial y^2} + \frac{\partial^2 \varphi}{\partial x^2} = 0 \quad (1)$$

From this point on, the plate can be transformed into a circle by using a complex function method. Hence, the mathematics of the problem becomes a flow around a cylinder with a finite number of point vortices outside the circle. In this case, the complex potential expression of the flow is:

$$W(\zeta) = -\frac{i}{2} |V_\infty| \sin \alpha \left(\zeta - \frac{r^2}{\zeta} \right) - \sum_{j=1}^N \frac{i\sqrt{\Gamma_j}}{2\pi} \ln \frac{(\zeta - \zeta_j)(\zeta + \frac{r^2}{\zeta_j})}{(\zeta + \zeta_j)(\zeta - \frac{r^2}{\zeta_j})} \quad (2)$$

where the first term is the complex potential of a uniform incident flow around a cylinder and the second term is the complex potential generated by the finite number of point vortices and their image vortices outside the circle. The boundary conditions are automatically satisfied on the circle. The conformal mapping is:

$$X = \frac{1}{2} \left(\zeta + \frac{r^2}{\zeta} \right) \quad (3a)$$

$$\zeta = X + \sqrt{X^2 - r^2} \quad (3b)$$

It should be noted that in this transformation there is a magnifying factor $dX/d\zeta|_{\infty} = \frac{1}{2}$ at infinity. Therefore, $U_\infty' = 1/2 V_\infty \sin \alpha$. The diameter of the circle is the width of the plate.

In addition to surface boundary conditions, the Kutta condition must also be satisfied.

$$v - i\omega \Big|_{z \rightarrow \infty} = \frac{d}{dX} W(X) \Big|_{z \rightarrow \infty} = \frac{dW(\zeta)}{d\zeta} \frac{d\zeta}{dX} \Big|_{z \rightarrow \infty} \rightarrow \infty \quad (4)$$

Because $d\zeta/dX \rightarrow \infty$ at the edge of the wing, therefore, we must have $dW(\zeta)/d\zeta = 0$. Hence, we get

$$\sum_{j=1}^N \frac{\Gamma_j}{2\pi} \left\{ \frac{\zeta_j}{\zeta_j^2 - r^2} + \frac{\zeta_j}{\zeta_j^2 - r^2} \right\} = \frac{1}{2} |V_\infty| \sin \alpha \quad (5)$$

The point vortex moves downstream at the local velocity. Therefore, we must also find the velocity of every point vortex.

If the velocity of the k th vortex is expressed as:

$$v_k - i\omega_k = \frac{dW(X)}{dX} \Big|_{x=x_k} + \frac{d}{dX} \left[\frac{i\Gamma_k}{2\pi} \ln(X - x_k) \right] \Big|_{x=x_k}, \quad k = 1, 2, \dots, N. \quad (6)$$

where the second term on the right indicates that the inducing velocity of the k th vortex itself should be subtracted from the calculation of the velocity at the k th vortex because it is a velocity singular point. After using equations (2) and (3) to calculate, equation (6) becomes

$$v_k - i\omega_k = (G_1 + G_2 + G_3) \frac{d\zeta}{dX} \Big|_{x_k} + G_4 \quad (7)$$

where

$$G_1 = -\frac{i}{2} |V_\infty| \sin \alpha \left(1 + \frac{r^2}{\zeta_k^2} \right),$$

$$G_2 = -\sum_{j=1}^N \frac{i\Gamma_j}{2\pi} \frac{1}{\zeta_k - \zeta_j},$$

$$G_3 = -\sum_{j=1}^N \frac{i\Gamma_j}{2\pi} \left(\frac{1}{\zeta_k + \frac{r^2}{\zeta_j}} - \frac{1}{\zeta_k + \zeta_j} - \frac{1}{\zeta_k - \frac{r^2}{\zeta_j}} \right),$$

$$G_4 = \frac{i\sqrt{k}}{2\pi} \frac{r^2}{\zeta_k^2 \left(1 - \frac{r^2}{\zeta_k^2} \right)}, \quad \frac{d\zeta}{dX} \Big|_{x_k} = \frac{2}{1 - \frac{r^2}{\zeta_k^2}}$$

Intensity and Position of Newly Generated Leading-edge Vortex

In the unsteady flow analogy, the leading-edge vortex is approximated by many discrete vortices. Newly generated vortices continue to be separated from the edge of the wing into the flow field with time. Therefore, the number of vortices continues to increase in the flow field. The intensity of a newly generated vortex has a great effect on the shape and position of the rolling-up of the leading-edge vortex and the surface pressure distribution. Many authors have investigated this problem. The

variation of the vortex flow in the shear layer near a leading-edge separation point with time is:

$$\partial \Gamma / \partial t = \frac{1}{2} (V_{\text{down}}^2 - V_{\text{up}}^2) \quad (8)$$

where V_{up} and V_{down} represent the velocities at the upper and lower surface of the shear layer near a separation point.

According to Sacks^[4] method, let $V_s = \frac{1}{2}(V_{\text{up}} + V_{\text{down}})$, i.e., the average velocity of the shear layer which is also the velocity at which the shear layer is dragged out the edge of the wing. $\gamma_x = V_{\text{down}} - V_{\text{up}}$ is the vortex intensity on a unit length. Based on these, equation (8) can be re-written as:

$$\Delta \Gamma = \Delta t \cdot (V_s \gamma_x) = (V_s \Delta t) \cdot \gamma_x = \Delta s \cdot \gamma_x \quad (9)$$

Δs is the length of the shear length dragged out in Δt time. The expression for V_s is found to be

$$v - i\omega \Big|_z = \sum_{j=1}^N \frac{is\Gamma_j}{2\pi} \left[\frac{\xi_j}{(\xi_j - z)^2} - \frac{\xi_j}{(\xi_j - \bar{z})^2} \right] \quad (10)$$

Because of symmetry, w_s is equal to zero in practice. There is only a y-direction velocity which shows that the shear layer is dragged out tangentially from the leading-edge. In our computation, v_s was found with equation (10) in order to determine the vortex layer length Δs . Then, the simplified point vortex is centered in this section of vortex layer so that the intensity of the newly generated vortex could be determined by using the Kutta condition.

Surface Pressure Distribution and Attached Vortex Line

From the definition of the pressure coefficient $c_p = (P - P_\infty) / \frac{1}{2} \rho U_\infty^2$, we get

$$c_p = \sin^2 \alpha - \frac{2\phi_x \cos \alpha}{V_\infty} - \frac{\phi_x^2 + \phi_y^2 + \phi_z^2}{V_\infty^2} \quad (11)$$

where $\phi_y = v$, $\phi_x = w$, $\phi = R.P.[W]$. The calculation of ϕ_x must take two aspects into account. One is that the semi-wing span $s(x)$ is a function of x . The variation caused by $s(x)$ is $\phi_x = ds(x)/dx \cdot R.P.[W(X)/ds]$. The other is ϕ_x caused by the variation of the point vortices with x . The derivation of the entire formula is tedious. It is omitted here. On the wing surface, $\phi_x = 0$. The attached vortex line on the wing surface can be determined based on the following

$$\gamma = n \times (V_{up} - V_{down}) \quad (12)$$

γ is the attached vortex vector on the wing surface. Let γ_x and γ_y be the components of γ in the x and y directions, respectively. $\gamma = \gamma_x i + \gamma_y j$. Then, $\gamma_x = -(\phi_{yup} - \phi_{ydown})$, $\gamma_y = \phi_{xup} - \phi_{xdown}$, where ϕ_{xup} , ϕ_{xdown} , ϕ_{yup} , and ϕ_{ydown} are the velocity components on the upper and lower wing surface.

After the attached vortex line on the wing surface is found, it is very easy to obtain the intensity of the trailing-edge tail vortex. Due to the fact that $\gamma_x = -\partial \Gamma / \partial y$, the intensity of the i^{th} tail vortex as a result of trailing-edge discretization is

$$(\Delta \Gamma_i)_{trailing-edge} = \int_{y_i}^{y_{i+1}} (\gamma_x)_{trailing-edge} dy \quad (13)$$

III. Brief Description of Results of Computation

Mathematically, this computation is to solve a variable number of first order normal differential equations. We can use the Runge-Kutta method to calculate gradually from the apex of

the wing downstream. With each increasing step, a new vortex is generated,

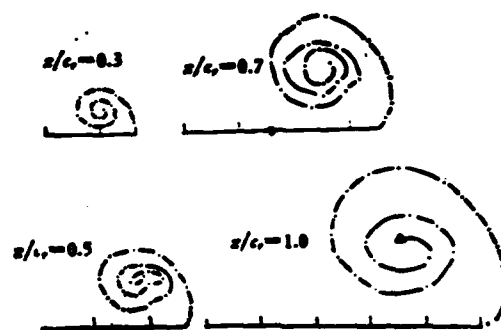


Figure 5. Rolling-up of Leading-edge Vortex on Top of Wing Surface

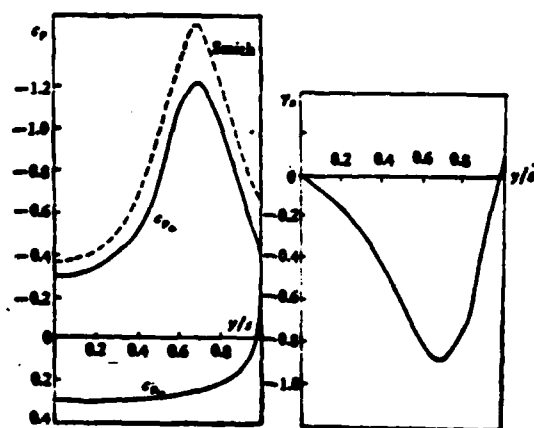


Figure 6. Surface Pressure Distribution and Attached Vortex Distribution (Trailing-edge of the Wing)

resulting in two additional equations. When calculating the /459
trailing-edge, the intensity of the trailing-edge vortex is found
and combined into the original equation to be moved downstream.

In order to compare with the experiment, we calculated a
delta wing whose aspect ratio $A=1.0$ and attack angle $\alpha=20.5^\circ$.
Figure 5 shows the gradual rolling-up of the leading-edge vortex
over the upper wing surface. Figure 6 shows the pressure
distribution and attached vortex intensity distribution at the
trailing-edge. The pressure distribution is very close to that
calculated by Smith. However, it is different from the
experimental result (see Figure 2). From the experimental result
one can see that the flow in the front part of the delta wing
approaches the conical flow assumption. However, the rear part,
especially near the trailing-edge, is no longer a conical flow.
The suction peak decreases with increasing x . But, this tendency
cannot be calculated using a two-dimensional model. This is
because the two-dimensional model does not meet the trailing-edge
Kutta condition. Although the load distribution on the wing
surface can be more accurately calculated based on a three-
dimensional flow model using a higher order surface element "free
vortex layer" method currently under development, yet it takes
too much computing time. As a qualitative analysis, we chose the
two-dimensional model.

From the distribution of attached vortex intensity along the
span γ_x one can see that γ_x is negative over most of the wing
span. It is positive near the edge of the wing. In addition,

under the leading-edge vortex, γ_x has a negative maximum. According to the calculated result reported in reference [9], a vortex will be rolled-up at the extremum $|\gamma_x|$. When γ_x is negative, the vortex rolled-up is clockwise.

Figure 7 shows the rolling-up of leading-edge and trailing-edge vortices and their interaction. For comparison, Hummel's experimental results are again shown in Figure 8. From the figures, the two situations are quite similar. In Figure 7(a), the trailing-edge vortex layer already begins to fluctuate. It bulges slightly at the extremum $|\gamma_x|$ and develops downstream. On one hand, it continues to bulge and enlarge and gradually rolls up into a clockwise vortex. On the other hand, because of the side wash velocity effect induced by the leading-edge vortex, the trailing-edge vortex layer extends in the direction of the wing edge. The vortex rolled up by the trailing-edge moves outward. It is initially on the right lower side of the leading-edge vortex and then gradually rises. From the figure one can also see that the trailing-edge vortex begins to roll up at approximately $1/4$ of a wing span ($x/c_r=1.10$) from the trailing-edge. At $1/2$ wing span ($x/c_r=1.20$), it has already developed well.

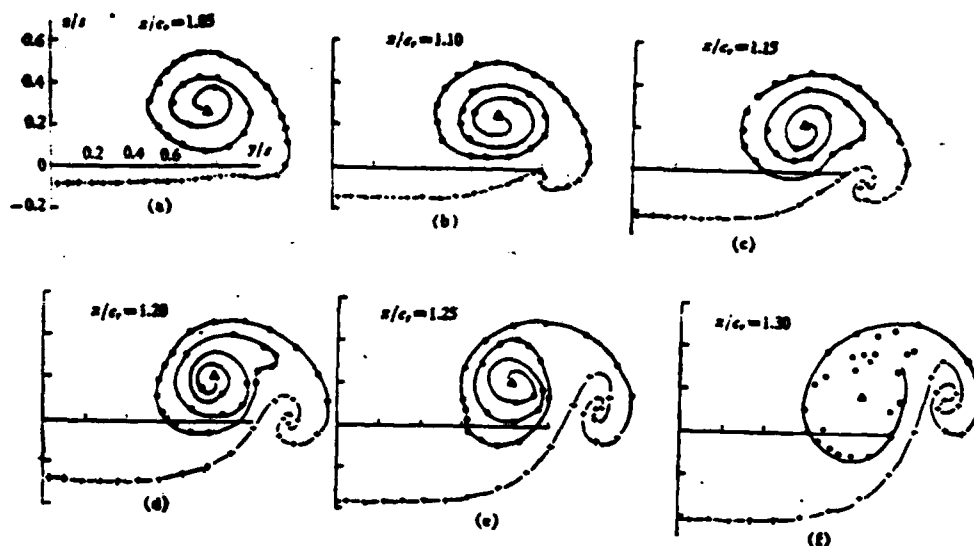


Figure 7. Rolling-up of Leading-edge and Trailing-edge Vortex Layers Downstream from Trailing-edge of the Wing

In order to study the effect of the leading-edge vortex on the trailing-edge vortex, we also did two interesting numerical experiments. Figure 9 shows the effect of the leading-edge vortex layer. We artificially neglected the vortex layer and /460 consolidated the leading-edge as a point vortex. The consolidation is based on the conservation of vortex moment and circulation. In the figure, the symbol Δ represents the consolidated leading-edge vortex. We found in the figure that the trailing-edge vortex could also roll-up a vortex. However, the shape and position are quite different from those shown in Figures 7 and 8. Thus, the effect of the leading-edge vortex layer cannot be neglected.

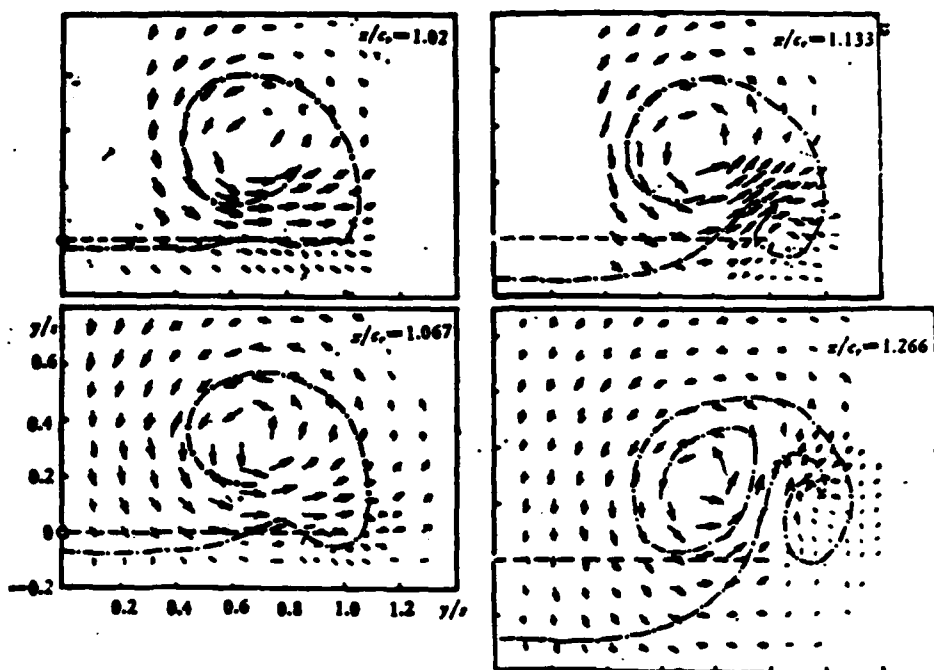


Figure 8. Hummel's Experimental Results^[3]

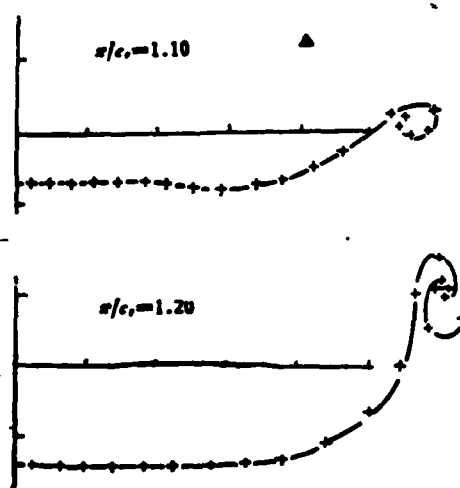


Figure 9. Rolling-up of Trailing-edge Vortex When Leading-edge Vortex is Consolidated into a Point Vortex

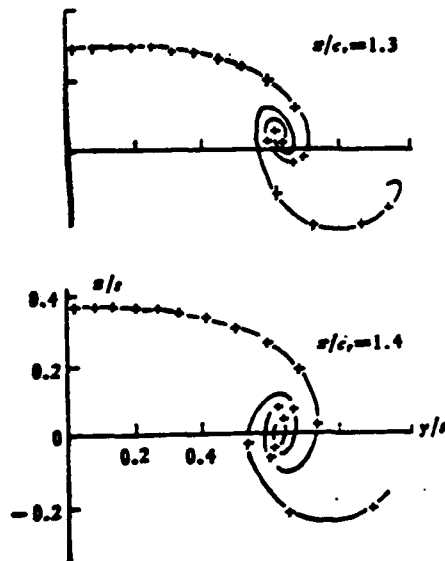


Figure 10. Rolling-up of Trailing-edge Vortex When Neglecting Leading-edge Vortex

Figure 10 shows the rolling-up of the trailing-edge vortex /461 when the entire leading-edge is neglected. Just as expected, a clockwise vortex is rolled-up at the extremum $|y_x|$. A counterclockwise vortex is rolled-up at the wing tip. Because the γ_x value is very small at the wing tip, only a small vortex is rolled-up. In addition, the number of point vortices is not sufficient to see clearly. Because of the absence of the leading-edge vortex side wash velocity effect, the trailing-edge vortex layer extends slowly. The clockwise vortex is on the inside of the wing tip vortex.

IV. Conclusions

In this work, a two-dimensional discrete vortex model was established based on the two-dimensional unsteady analogy. Numerical simulation of Hummel's experimental results was realized on a computer. The rolling-up of the leading-edge and trailing-edge vortices and the results of their interaction thus obtained are very similar to Hummel's experimental results. It proves that it is basically feasible to study the mechanism using a two-dimensional model. Major physical pictures of the flow field can be obtained.

1. In addition to the vortex rolled up by the leading-edge vortex downstream, the trailing-edge vortex will roll up another vortex. The circulations of these two vortices are opposite.

2. Under the influence of the side wash velocity induced by the leading-edge vortex, the trailing-edge vortex layer extends toward the edge of the wing. Initially, a vortex is rolled up on the lower right side of the leading-edge vortex. Then, as the circulation gradually increases, it rises comparatively. The presence of the leading-edge vortex accelerates the rolling-up process of the trailing-edge vortex and also pulls it outward.

3. The wash flow field is complicated where there are leading-edge and trailing-edge vortices present. There is a need to understand it better. This study has helped the understanding of the physical picture of the wash flow field. However, because of the characteristic deficiencies of the two-dimensional model, there are discrepancies in the quantitative determination of the

pressure distribution on the wing surface. A more complex three-dimensional vortex layer model must be used to more accurately calculate the pressure distribution on the wing surface. This work is just a preliminary investigation.

After this paper was sent for review, we discovered two similar studies done abroad. Kandil^[10] used a vortex lattice method to calculate a three-dimensional flow field. But, the structure of the rolled-up vortex layer is not clear. The work done by Hoeijmakers^[1,2] et al. is similar to ours. They also used a two-dimensional vortex layer model to obtain similar results. However, the methodology is not quite the same. On the wing surface and in the vortex layer, they used dipole distribution, vortex layer shape and wing surface dipole strength distribution and solved them by iteration. We established a series of point vortex equations through conformal mapping to convert it to a problem of solving for initial values.

References

- [1] Brown, C.E. and Michael, W.H., J. Aero. Sci., 21 (1954), 690-694.
- [2] Mangler, K.W. and Smith, J.H.B., Proc. Roy. Soc. Lond, A 251 (1959), 200-217.
- [3] Smith, J.H.B., Proc. Roy. Soc. Lond, A 306 (1968), 67-90.
- [4] Sacks et al, NASA CR-719 (1968).
- [5] БелыепкоБекHH, C.M., H36. AH CCCP, MKT, 4 (1968).

- [6] Kandil, O.A., Mook, D.T., Nayfeh, A.H., J. Aircraft, 13 (1976), 22-28.
- [7] Rubbert, P.E., AIAA paper 76-147 (1976).
- [8] Hummel, D., AGARD conf. Proc. 247 (1978), s.15-1 bis 15-17.
- [9] Yin Xieyuan and Deng Guohua, Journal of University of Science and Technology of China, 12, 4 (1982), 91.
- [10] Kandil, O.A., AIAA paper 81-1263.
- [11] Hoeijmakers, H.W. & Vaatstra, W., AIAA.J, 21, April (1983).
- [12] Hoeijmakers, H.W., Vaastra, W., Verhaagen, N.G., J. Aircraft, Sept. (1983).

INVESTIGATION OF ROLLING-UP AND INTERACTION OF LEADING-EDGE AND TRAILING-EDGE VORTEX SHEETS ON A SLENDER DELTA WING

Yin Xieyuan, Xia Nan, Deng Guohua
(University of Science and Technology of China)

Abstract

Hummel's experiment on the rolling-up and interaction of the leading-edge and trailing-edge vortex sheets at slender delta wing is modeled numerically by a simple two-dimensional theory. The numerical results show that the trailing-edge vortex sheet will roll-up at the downstream of the wing, in the presence of the leading-edge vortex, and the direction of the circulation of the leading-edge vortex is oppsite to the trialing-edge vortex. The numerical results are in good agreement with the experiment. This work is important to further understand of the downstream flow-field of a wing.

Calculation of Circular Jet with Particles Impacting
Upon a Plate

/463

Liu Dayou
(Institute of Mechanics, Academia Sinica)

Abstract

Under the inviscid and incompressible flow condition, the flow field of a uniform circular jet with particles impacting upon an infinite plate is calculated. In addition, two drag coefficient formulas, i.e., $24/Re$ and $24/Re (1+Re^{2/3})$, are used to calculate the trajectories of spherical particles in the flow field. Assuming particles are uniformly distributed in the jet outlet, the impact coefficient $P(S_t, \Omega^*)$ curve (known as the collection probability in the study of samplers) has been obtained. The rationale of each assumption is discussed. The effect of viscosity is discussed. The $P(S_t, \Omega^*)$ curve is corrected for the effect of viscosity. Results indicate that impact points are mainly concentrated in the $X < 2$ region on the plate. Although it is assumed to be very large in the calculation, however, the results are still applicable to the situation $H=1.5$. Experimentally, it has been proven that samplers designed based on the $P(S_t, \Omega^*)$ curve calculated in this work can realize anticipated specifications.

As ecological science develops, there is a need to study the effect of particles of various diameters in the atmosphere on human health. Therefore, in addition to the need to know the total mass density and number density of particles in the atmosphere, it is also required to know the particle diameter

distribution. To this end, many nations are developing various atmospheric particle collectors capable of sorting by diameter. One of the most common types is the impact sampler which is based on fluid dynamics principles^[1]. The basis for studying the collection probability of an impact sampler is to determine the particle trajectory of a jet impacting upon a plate.

Based on the inviscid and incompressible fluid assumption, the flow field of a uniform jet impacting upon an infinite plate and the spherical particle trajectory in the flow field are calculated. The impact coefficients P of various diameters (also know as collection probabilities in the study of samplers) were determined. The rationale for each assumption made in the calculation was discussed. Moreover, some corrections were made based on the actual flow to finally obtain the $P(S_t, \Omega^*)$ curve for the design of samplers.

I. Basic Assumptions and Dimensional Analysis

If a gas flow is injected out of the round hole CC toward the plate AA (as shown in Figure 1), the streamline (CB,PQ) bends as it is passing through the plate. Both magnitude and direction of velocity change. At a distance from the axis, such as the flow along the plate near B and Q, the velocity is close to the exit velocity v_{∞} . The particles in the flow move along with the gas in the hole. When the streamline bends, the velocity of the particle lags behind that of the gas due to inertia. Therefore, the trajectory of the particle, such as PQ', deviates from the

streamline. The inertia varies with particle diameter and density. Therefore, the extent of deviation is also different. Some particles impact the plate and some flow through the hole in the next stage.

Assumption (1): The flow is incompressible and inviscid. Moreover, the effect of gravity is neglected.

Assumption (2): The particle velocity has already caught up with the flow velocity before reaching the jet outlet. It is in equilibrium. Particles are uniformly distributed in the flow. At the jet outlet, the flow velocity is uniform.

Assumption (3): The effect of diffusion is neglected.

Manuscript received on February 4, 1983.

/464

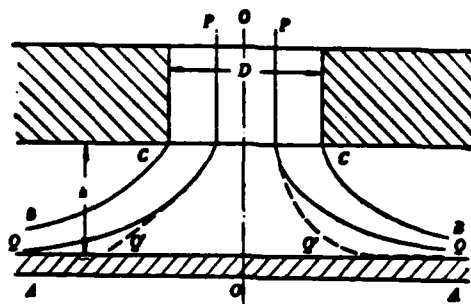


Figure 1

Assumption (4): The particle content is very small and the presence of particles does not affect the flow field.

Parameters affecting the motion of particles are:

D - aperture diameter, v_{∞} - jet velocity,
 ρ - gas density, μ - aerodynamic viscosity coefficient,
 ρ_p - density of particle material, d - particle diameter,
 $2s$ - collector plate diameter, h - impact distance,
 g - gravitational acceleration, a - speed of sound,
 λ - mean free path of gas molecule,
 x_{p0} - initial value of radial coordinate of the particle
 x_p (i.e., at the outlet of the jet),
 t - time.

Let A represent a function of the velocity components of the particle u_p and v_p or the coordinates of the particle x_p and y_p . Its general form is

$$A = f_0(D, v_{\infty}, \rho, \mu, \rho_p, d, 2s, h, g, a, \lambda, x_{p0}, t)$$

When studying the trajectory of a particle, then

$$x_p = f(D, v_{\infty}, \rho, \mu, \rho_p, d, 2s, h, g, a, \lambda, x_{p0}, y_p)$$

The parameters in the above formula are rendered non-dimensional by using D , v_{∞} and ρ . By taking assumptions (1) and (2) into account, we get:

$$X_p = F\left(\Theta, \textcircled{R} \frac{d}{D}, S, H, K_n, X_{p0}, Y_p\right)$$

where $\textcircled{R} = \rho D v_{\infty} / \mu$ (Reynolds number) $K_n = \lambda / d$ (Kenuzhen Constant)

$$\Theta = \frac{R}{18} \cdot \frac{\rho_p}{\rho} \cdot \frac{d^2}{D^2},$$

$$S = 2s/D,$$

$$X_p = 2x_p/D,$$

$$H = 2h/D,$$

$$X_{p0} = 2x_{p0}/D,$$

$$Y_p = 2y_p/D.$$

In the limiting case that both H and S are very large, the above formula is simplified as:

$$X_p = G\left(S, \frac{d}{D}, K_n, X_{p0}, Y_p\right)$$

The impact point of the particle on the collector plate is

$$X_{p0} = G\left(S, R, \frac{d}{D}, K_n, X_{p0}, 0\right)$$

When $X_{p0} \rightarrow \infty$, $X_{p0} \rightarrow (X_{p0})_{cr}$. Then

$$(X_{p0})_{cr} = Q\left(S, \frac{d}{D}, K_n\right)$$

Because of Assumption (2), the impact coefficient $P = (X_{p0})_{cr}^2$. It /465 represents the ratio of the number of particles at a certain diameter collected on the collector plate to the total number of such particles. In sampler studies, it is called the relative collecting probability^[7]. Computation shows that the solution obtained with a very large H is still appropriate at $H=1.5$. In the following, functions G and Q are determined numerically based on fluid dynamic equations.

II. Basic Equations and Boundary Conditions of the Flow Field

In an axi-symmetric coordinate system, the velocity potential ϕ of an inviscid and incompressible flow satisfies the following equations:

$$\frac{\partial^2 \phi}{\partial x^2} + \frac{\partial^2 \phi}{\partial y^2} + \frac{1}{x} \frac{\partial \phi}{\partial x} = 0$$

$$u_r = \frac{\partial \phi}{\partial x} \quad v_r = \frac{\partial \phi}{\partial y}$$

where x is the radial coordinate and y is the axial coordinate. The subscript g indicates gas. CD and AB are equi-potential surfaces. DO and OA are zero flow lines. CB is the free boundary of the jet (see Figure 2). The boundary conditions are:

$$\psi = \text{constant (i.e., } u_g=0, v_g=-v_\infty) \text{ on CD}$$

$$\psi = \text{constant (i.e., } u_g=v_\infty, v_g=0) \text{ on AB}$$

$$\psi = \text{constant (i.e., } n_1 \cdot \nabla\psi=0), \tau_1 \cdot \nabla\psi=v_\infty \text{ on BC}$$

$$\psi = 0 \text{ (i.e., } n_1 \cdot \nabla\psi=0) \text{ on DO and OA.}$$

where ψ is the flow function, n_1 is the unit vector in the normal direction and τ_1 is the unit vector in the tangential direction.

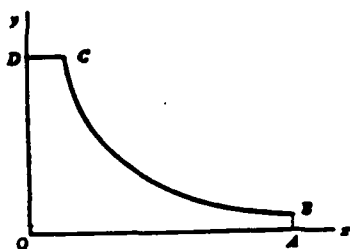


Figure 2

$D/2$ is used as the characteristic length and v_∞ is the characteristic velocity to render the above equations non-dimensional:

$$\frac{\partial^2 \psi}{\partial X^2} + \frac{\partial^2 \psi}{\partial Y^2} + \frac{1}{X} \frac{\partial \psi}{\partial X} = 0 \quad (2.1)$$

$$\partial \psi / \partial Y = -1 \quad \text{along CD} \quad (2.2)$$

$$\partial \psi / \partial X = 1 \quad \text{along AB} \quad (2.3)$$

$$n \cdot \nabla \psi = 0, \tau \cdot \nabla \psi = 1 \quad \text{along BC} \quad (2.4)$$

$$n \cdot \nabla \psi = 0 \quad \text{along DO, OA} \quad (2.5)$$

The velocity components are:

$$u = -\frac{\partial \phi}{\partial x} \quad v = -\frac{\partial \phi}{\partial y} \quad (2.6)$$

where n and τ are the unit vectors in the normal and tangential direction on the XY plane.

This is a Laplace equation with unknown boundary BC. By using the characteristics of the harmonic function, the Green function is introduced to convert the above differential equation to an integral equation. Under specific conditions, it can be integrated. This is the so-called point source function method in fluid dynamics.

The unknown boundary \overline{BC} can be assumed to be a known curve. The velocity potential $\phi_1(t)$ of various points on \overline{BC} and the potential velocity of points on DC and AB are calculated. Furthermore, the velocity potential of points on OA is also calculated. Based on the integral expression of velocity potential, the velocity potential $\phi_2(t)$ of points on \overline{BC} can be calculated. The shape \overline{BC} can be repeatedly adjusted until $\phi_1(t) = \phi_2(t)$ [2].

In our calculation, we chose $Y(C) = Y(D) = 3$. In this case, at $X(A) = x(B) = 4$, the flow velocity is already very uniform. /466 Moreover, the non-dimensional velocity ≈ 1 . The result of this calculation is shown in Figure 3.

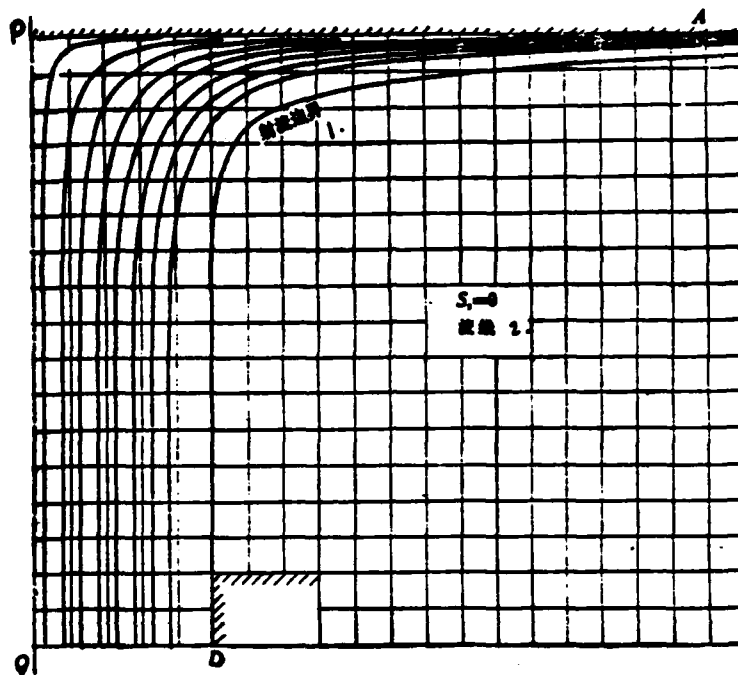


Figure 3. Streamlines of Spherical Particle Jet Impacting Upon a Plate

1. jet boundary
2. streamline

III. Equation of Motion of the Particle, Initial Conditions and Integration of Equations

1. Equation of Motion and Initial Conditions

The equation of motion of a particle in a known flow field is:

$$\frac{\pi}{6} d^3 \rho_p \frac{d w_p}{d t} = \frac{\pi}{4} d^2 \cdot C_D \cdot \frac{1}{2} \rho w_{1p} \cdot w_{1p} \quad (3.1)$$

$$\frac{d r_p}{d t} = w_p \quad (3.2)$$

where

$$w_{gp} = w_g - w_p \quad (3.3)$$

$$w_{gp} = |w_{gp}| \quad (3.4)$$

w_g and w_p are the velocity vector of the primary flow and the velocity vector of the particle, respectively.

r_p is the particle position vector.

t is the time.

For a small particle, the drag coefficient C_D can be expressed as

$$C_D = \frac{24}{Re} f(Re) / \omega \quad (3.5)$$

where $Re = d \cdot p \cdot w_{gp} / \mu$ which is the Reynolds number of the particle^{/467} based on using the particle diameter d as the characteristic length and relative velocity w_{gp} as the characteristic velocity.

$$w = 1 + 2.46\lambda/d \quad (3.6)$$

where w is a correction factor for the dilute gas effect and λ is the mean free path of the gas molecule. Obviously, when $\lambda \ll d$, $w=1$.

In this calculation, we chose $f(Re)=1$ and $f(Re)=1+1/6Re^{2/3}$.

Therefore,

$$C_D = \frac{24}{\omega Re} \quad (3.7a)$$

and

$$C_D = \frac{24}{\omega Re} (1 + Re^{2/3}) \quad (3.7b)$$

Equations (3.1) and (3.2) are made non-dimensional by using $D/2$ and v_∞ as the characteristic quantities.

$$\frac{dW_r}{dT} = \frac{f(Re)}{2S_r} (W_\infty - W_r) \quad (3.8)$$

$$\frac{dR}{dT} = W, \quad (3.9)$$

where

$$T = 2v_{\infty}t/D \quad (3.10)$$

$$S_t = w \textcircled{H} \text{ (Stokes number)} \quad (3.11)$$

$$\Theta = \frac{\tau_v \cdot v_{\infty}}{D} = \frac{R}{18} \cdot \frac{\rho_p}{\rho} \cdot \frac{d^2}{D^2} \quad (3.12)$$

$$R = \frac{\rho D v_{\infty}}{\mu} \quad (3.13)$$

$$W_r = w_r/v_{\infty} \quad (3.14)$$

$$W_t = w_t/v_{\infty} \quad (3.15)$$

$$W_{tr} = W_t - W_r \quad (3.16)$$

$$R_p = 2r_p/D \quad (3.17)$$

The relation between R and Re is:

$$Re = R d/D |W_{gp}| \quad (3.18)$$

τ_v is the relaxation time used to judge the lagging of the particle velocity variation behind the flow velocity variation.

\textcircled{H} and S_t can be considered as non-dimensional relaxation times. From equation (3.8) we can see that when S_t is very small, i.e., when the relaxation time is very short, the velocity of the particle and that of the flow are in equilibrium. Otherwise, it is not in equilibrium.

When cartesian coordinates X and Y are used on the azimuthal plane, the equations become

$$\frac{dU_p}{dT} = \frac{f(R_p)}{2S_t} (U_s - U_p) \quad (3.19)$$

$$\frac{dV_p}{dT} = \frac{f(R_e)}{2S_e} (V_e - V_p) \quad (3.20)$$

$$\frac{dX_p}{dT} = U_p \quad (3.21) \quad /468$$

$$\frac{dY_p}{dT} = V_p \quad (3.22)$$

$$\text{when } T=0, U_p=0, V_p=-1, X_p=X_{p0}, Y_p=Y(C) \equiv H \quad (3.23)$$

U_p, V_p and U_g, V_g are the X, Y components of W_p and W_g , respectively. X_p and Y_p are the components of R_p .

On the meridian plane, if the potential function Φ and flow function Ψ are expressed in an orthogonal coordinate system, then the equations become

$$\frac{dW_{\tau}}{dT} = \frac{f(R_e)}{2S_e} (W_e - W_{\tau}) - W_{\tau} \frac{d\alpha}{dT} \quad (3.24)$$

$$\frac{dW_n}{dT} = W_{\tau} \frac{d\alpha}{dT} - \frac{f(R_e)}{2S_e} W_{\tau} \quad (3.25)$$

$$\frac{d\Phi_p}{dT} = W_{\tau} / \beta_\Phi \quad (3.26)$$

$$\frac{d\Psi_p}{dT} = -W_{\tau} / \beta_\Psi \quad (3.27)$$

$$\text{When } T=0, W_{p\tau}=1, W_{pn}=0, \Phi_p=\Phi(C) \equiv A, \Psi_p=\Psi_{p0} \quad (3.28)$$

where $W_{p\tau}, W_{pn}, \Phi_p$ and $(-\Psi_p)$ are the components of W_p and R_p in the direction of τ and n , respectively. τ is the unit vector in the tangential direction of the streamline pointing in the direction of increasing Φ . n is the unit vector in the streamline direction pointing in the direction of decreasing Ψ . α is the angle of rotation from the x -axis counterclockwise to τ -direction. The problem is that $\alpha < 0$.

2. Integration of Equation of Motion of Particles

(1) Method of Integration

For a very small particle (e.g., $S_t < 0.05$), because its trajectory of motion almost coincides with the streamline, it is possible to employ a perturbation method. When $(2S_t)^2$ is very small (in general $f(Re) \approx 1$) and $d^2 U_p / dT^2$ is not very large, we get the following from equation (3.19)

$$U_s \approx U_s - \frac{2S_t}{f(Re)} \left[U_s \frac{\partial U_s}{\partial X} + V_s \frac{\partial U_s}{\partial Y} \right] \quad (3.29)$$

A similar expression can be obtained for V_p .

If ΔT (step length) = 0.15, when $0.01 < S_t < 0.075$, equations (3.19) - (3.22) can be integrated using the Treanor method^[3]. In our computation, it was proven that the results obtained with Treanor's method are in total agreement with those obtained with the perturbation method at $S_t = 0.01$ and $\Delta T = 0.15$.

When $S_t > 0.075$, the R-K method can be used.

For very small particles, a larger step can be used in the perturbation method. In this case, it is more appropriate to use the ψ - η coordinate because W_{pn} is very small and W_{pr} does not vary significantly.

Thus, a series of particle trajectories can be calculated corresponding to any given S_t and $R d/D$. Taking the requirements of sampler design into account, we used n^* to replace $R d/D$:

$$n^* = (R d/D) / S_t \quad (A)$$

(2) Selection of Step Length

In addition to considering requirements of satisfying the /469 stability of the difference scheme and the accuracy of the computation, we should try to shorten the computing time to the extent possible in order to make it practical. In this calculation, we chose $\Delta T=0.15$. The average time to calculate a trajectory is 60 seconds (on a Model FILEX-512 general purpose computer). Table 1 shows the Y value at $x=4$ on each trajectory when $S_t=0$ (in this case, trajectories are streamlines). These values were compared to those corresponding to $Y=1/8X_{p0}^2$ ¹⁾ and were found in good agreement. This demonstrated that the required accuracy is satisfied in the calculation.

Table 1

表 1

x_{p0}	0.05	0.15	0.25	0.35	0.45	0.55	0.65	0.75	0.85
$\frac{1}{8} x_{p0}^2$	0.0003125	0.0028125	0.0078125	0.01532	0.02530	0.037813	0.0528	0.0703	0.0903
1. 计算 Y	0.000303	0.00272	0.007568	0.01488	0.02456	0.036972	0.0518	0.0690	0.0894

1. calculated Y value

1) When $x=4$, $U_g=1$. From conservation of flow we get $Y=1/8X_{p0}^2$.

(3) Several Measures to Cut Down Computing Time

It took more than 10 minutes to calculate each trajectory using the initial program. The following measures were taken to reduce it to less than 1 minute.

(a) Frequently used elliptical integrals are calculated by series expansion to drastically save time and obtain good accuracy.

(b) Computation of Flow Velocity and its Partial Derivatives

For $Y > 0.03$, the flow velocity is calculated based on its integral expression. For $Y \leq 0.03$, the flow velocity at any point is calculated by series expansion. Not only time is saved but also accuracy is improved. Our computation showed that the series expansion method can be extended to $Y < 0.3$.

As for the calculation of various coefficients in the series expansion equation, i.e., U_g , $\partial U_g / \partial X$, $\partial^2 U_g / \partial X^2$, $\partial^3 U_g / \partial X^3$ at various points on the x-axis, the first two are calculated by using the integral expressions and the latter two are calculated first by using a sample value fitting method with discrete values of U_g and $\partial U_g / \partial X$ and then by differentiation.

We must point out here that even though a particle has already reached $Y=0.03$, we still cannot get the approximate value at $Y=0$ by extrapolation. When $Y \leq 0.03$, the particle trajectory bends significantly. Furthermore, for particles in the range of $S_t=0.1\sim 0.2$ (which is the range of our concern), V_p is very small when $Y=0.03$. Therefore, extrapolation is not reliable.

(c) The computation started from $Y=1.5$ due to the fact that the flow field is very uniform at $Y=2$ to $Y=3$, the plate has no effect on the jet, and the particle trajectory is straight.

IV. Analysis of Calculated Results

Figure 3 shows the streamlines. Figure 4 shows the calculated particle trajectories for $S_t=0.12$. If there is an arrow on a trajectory near the boundary OA, then this trajectory does not intersect with OA within $X<3.5$. Figure 5 shows the effect of α^* on the particle trajectory. Our computation shows that

/470

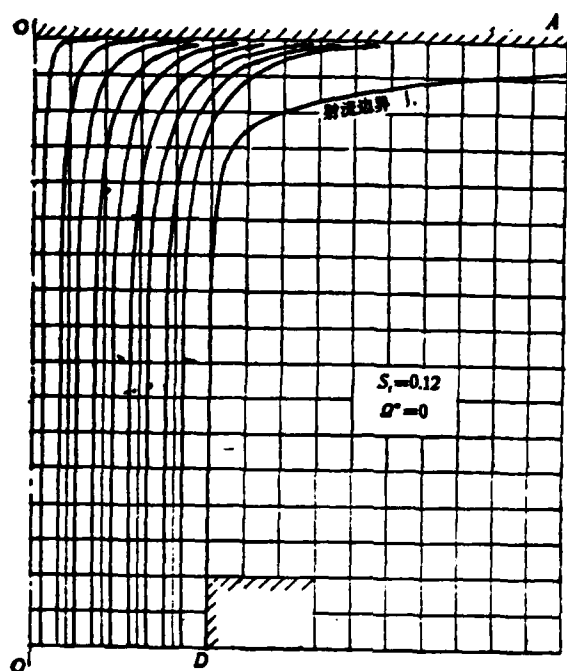


Figure 4. Particle Trajectories

1. jet boundary

(1) Within the range of $X < 3.5$, almost all the particles with $S_t < 0.11$ cannot reach the boundary OA unless X_{p0} is very small. Almost all particles with $S_t > 0.17$ can reach the OA boundary. Whether particles in the range of $0.11 < S_t < 0.17$ can reach the boundary OA at $X < 3.5$ depends on the values of X_{p0} and α *.

(2) Impact points are basically within $X < 2.0$. At $X > 2.0$, impact points are obviously frequent. This effect can be explained from equation (3.24) and (3.25).

The impact points of particles with large S_t are within $X = 2.0$. Let us now discuss particles with $S_t < 0.2$. In most areas of the flow field, $|\partial\alpha/\partial\Psi| \ll |\partial\alpha/\partial\Phi|$. For smaller particles, $W_{pn} \ll W_{pr}$. Thus

$$\frac{d\alpha}{dT} = \frac{1}{\beta_0} W_{pr} \frac{\partial\alpha}{\partial\Phi} - \frac{W_{ps}}{\beta_0} \frac{\partial\alpha}{\partial\Psi} \approx \frac{W_{pr}}{\beta_0} \frac{\partial\alpha}{\partial\Phi} = W_{pr}/R_\Psi \quad (4.1)$$

where R_Ψ is the radius of curvature of the streamline. By substituting equation (4.1) into (3.25), we get

$$\frac{dW_{ps}}{dT} = W_{pr}^2/R_\Psi - \frac{f(Re)}{2S_t} W_{ps} \quad (4.2)$$

By omitting the second term on the right of equation (3.24), we get

$$\frac{dW_{pr}}{dT} = \frac{f(Re)}{2S_t} (W_s - W_{pr}) \quad (4.3)$$

The first term on the right side of equation (4.2) represents the inertia centrifugal force which is the driving force to increase W_{pn} . The second term on the right represents the aerodynamic drag which is the damping force to decrease W_{pn} . When the centrifugal force can be neglected, W_{pn} decays exponentially.

The decay constant is $S_t (f(Re) \approx 1)$. The smaller the particle size is, the faster the decay becomes. For a microscopic gas group, $S_t = 0$. Thus, $W_{pn} = 0$. For a particle ($S_t > 0$), W_{pn} first gradually increases from zero and then gradually decays to zero. ψ_p is always decreasing. When $\psi_p = 0$, the particle reaches the collector plate.

/471

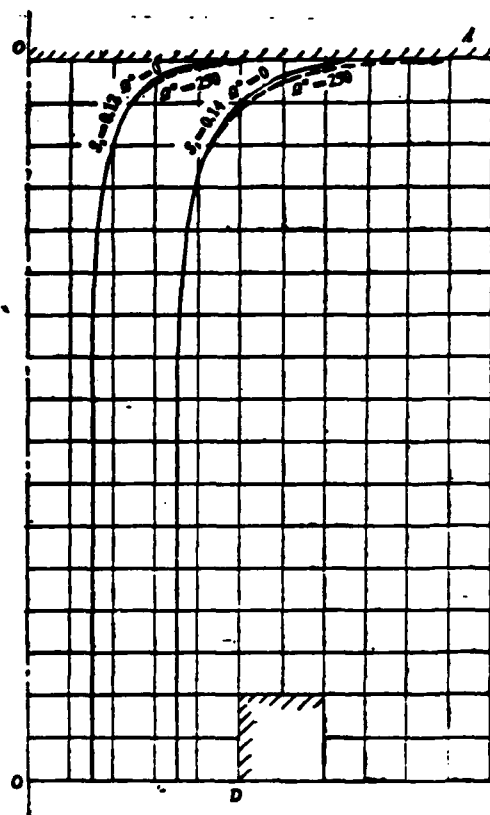


Figure 5. Particle Trajectories

$$\text{When } T=T_a, \quad W_{pn} \gg 2S_t W_{p\tau}^2 / R_{\Psi} \quad (4.4)$$

From (4.2) we get

$$W_{ps} = (W_{ps})_a \exp \left[-\frac{f(R_e)}{2S_t} (T - T_a) \right] \quad (4.5)$$

Substituting it into equation (3.27), we get

$$\Psi_p - (\Psi_p)_a = -\frac{2S_t}{f(R_e)} (W_{ps})_a \left\{ 1 - \exp \left[-\frac{f(R_e)}{2S_t} (T - T_a) \right] \right\} \quad (4.6)$$

The subscript a represents the value at $T=T_a$. When $(\Psi_p)_a$, $(W_{pn})_a$ and S_t are given, we can find the value of $(T-T_a)$ corresponding to $\Psi_p=0$ (see Table 2). When equation (4.4) is satisfied, usually $W_{p\tau} \approx U_p \approx 1$. Therefore, the second row in Table 2 corresponds to $(X_{pc} - X_{pa})/2S_t$. It is obvious from Table 2 that the impact points of a certain particle size are spaced less densely away from the center on the collector plate. This point was also experimentally verified.

Table 2

表 2

$(\Psi_p)_a/2S_t(W_{ps})_a$	0.6	0.7	0.8	0.9	0.925	0.95	0.97	0.99	1
$(T - T_a)/2S_t$	0.91	1.20	1.61	2.3	2.59	3.00	3.50	4.60	∞

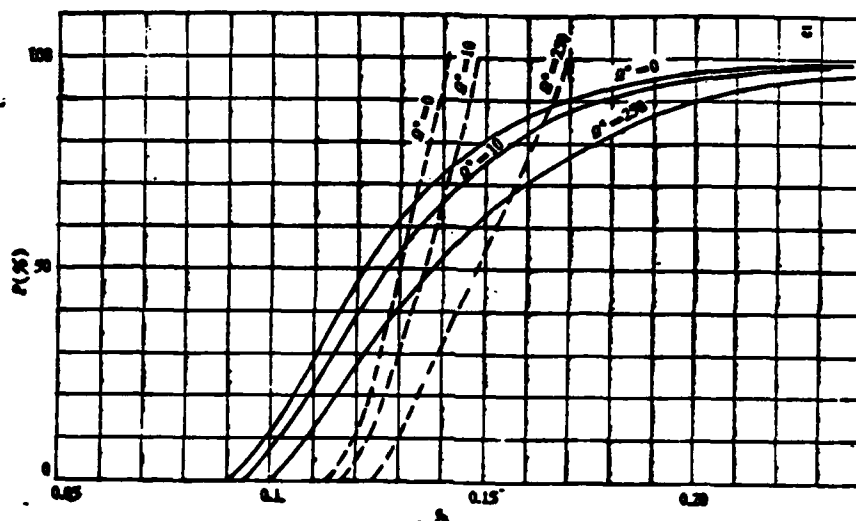


Figure 6. The $P(S_t, \alpha^*)$ Curve

1. not corrected for viscosity
2. corrected for viscosity

The above discussion indicates that the results of an infinitely large plate (i.e., S is very large) can be applied to a finite plate as long as the edge effect on the $X < 2.0$ region can be neglected.

(3) Corresponding to a specific S_t and α^* , there is a certain X_{p^0} (which is denoted as $(X_{p^0})_{cr}$) which corresponds to $X_{pe} = 3.5$.

From
$$p = (X_{p^0})_{cr}^2 \quad (4.7)$$

we can find the impact coefficient $p(S_t, \alpha^*)$ corresponding to that particular S_t and α^* .

V. Effect of Viscosity

When an impact type collector is used to collect particles larger than 1μ in diameter, the Ma number is usually less than 0.2 and Dg/v_∞^2 is less than 0.3. The flow field is a low Reynolds number laminar flow in which the effect of diffusion can be neglected. The accumulation of a few particles in the atmosphere will only affect the flow in the boundary layer. It has little effect on the inviscid flow field. Therefore, with the exception of neglecting the effect of viscosity, other assumptions made in performing the calculation are reasonable.

1. Analysis of Viscosity Effect

The effect of viscosity is primarily exhibited in three areas [4]:

- (1) Due to viscosity, the jet outlet velocity is non-uniform.
- (2) There is momentum exchange across the free boundary BC. Momentum is transferred from the inside to the outside of BC.
- (3) There is a boundary layer at the wall OA of the plate which makes U_g near OA smaller than the value in an inviscid flow. Due to the presence of the solid wall, the drag on the particle is also affected.

With regard to the effect of the first point, the following correction is made. Let us assume that the distribution of velocity at the outlet of the jet is:

$$\frac{v_x}{(v_x)_{\max}} = \left(1 - \frac{2x}{D}\right)^{1/2}$$

or

/473

$$\frac{v_{\infty}}{v_{\infty \max}} = 1.264 \left(1 - \frac{2x}{D}\right)^{1/6},$$

$(v_{\infty})_{\max}$ is the velocity at the center of the jet outlet. \bar{v}_{∞} is the mean velocity at the jet outlet. Hence

$$S_t / \bar{S}_t = 1.264 [1 - (X_{p^0})_{cr}]^{1/6}$$

where S_t is defined as $\tau_{v_{\infty}}/D$ and \bar{S}_t is defined as $\tau_v \cdot v_{\infty \max}/D$.

If we assume that the particle trajectory passing through a point at the outlet only depends on the local S_t value and is not related to the fact whether the jet is uniform or not, then the impact coefficient P is

$$P = \int_0^{(X_{p^0})_{cr}} v_{\infty} \cdot 2\pi X dX / \pi \bar{v}_{\infty} \\ = 1 - \frac{13}{6} [1 - (X_{p^0})_{cr}]^{7/6} - \frac{7}{6} [1 - (X_{p^0})_{cr}]^{13/6}.$$

With regard to the effect of item (2), because the flow velocity distribution near the boundary (jet mixing area) is affected by the momentum exchange across the free boundary, the particle trajectory is also altered. The half-width b of the mixing area at $H=1.5D$ was estimated by using the semi-infinite free jet formula^[4] (choosing velocity ratio = 0.95 as the jet boundary). It was found that $b/D/2$ is in the range of 0.22-0.093 which shows that the jet boundary only affects the $P>0.65-0.75$ portion of the $P(\bar{S}_t, n^*)$ curve.

With regard to the effect of item (3), due to the presence of the boundary layer near the wall, the transverse velocity near the wall is lower than that of an inviscid flow, which affects the flow of particles near the wall. For a collector operating

at a flow rate of 2 liter/min, the Reynolds number Re ranges from 626 (first stage) to 2606 (sixth stage). It is estimated that the ratio of the boundary layer thickness δ_0 to the radius of the jet $D/2$ ranges from 0.176 (first stage) to 0.080 (sixth stage). It is very small compared to $H=3$. In this thin layer, the streamline is already very straight. After a particle enters this thin layer, its normal direction velocity decays very rapidly. v_p will not drop significantly any further. Therefore, the effect of the boundary layer is mainly causing the tangential velocity of the particle to drop which consequently leads to an increase of time of particle motion. It has little effect on the shape of the particle trajectory¹⁾.

2. Corrected Results

The viscosity corrected impact coefficient $P(\bar{S}_t, \eta^*)$ curve is shown as the solid curve in Figure 6. When η^* varies from 0 to 250, $\bar{S}_{t,0}$ (the value of S_t corresponding to $P=50\%$) varies from 0.122 to 0.137. Corresponding to our calculating conditions, Marple and Wileke^[5] got $S_{t,0}=0.1165-0.11$ ²⁾ when $\eta^*=0$. R. Wiedemann^[6] chose $\sqrt{S_{t,0}}=0.343$ ³⁾ and got $S_{t,0}=0.11765$. In some foreign sampler designs, $S_{t,0}=0.144$ was chosen. These are in agreement with our computation.

The calculated $P(\bar{S}_t, \eta^*)$ curve was used to design a multi-stage impact sampler. After evaluation, it was found that the performance of the sampler agreed well with theoretical calculation. Design specifications are met^{[7]4)}.

1) More profound investigation not only requires the consideration of the inhomogeneity of velocity in the boundary layer but also must include, in addition to the drag in the direction of motion, the transversal force exerted on the particle by the flow.

2) In reference [5], $S_{tk,0}/2$ corresponds to $S_{t,0}$ in this work.

3) In reference [6], S_{tk} corresponds to $S_{t,0}$ in this work.

4) In reference [7], Θ_0 corresponds to $S_{t,0}$ in this work.

VI. Conclusions

When there are fewer particles in the jet, they do not affect the flow field significantly. Therefore, the computation of the particle trajectory and the flow field can be separately discussed. Under the inviscid and incompressible conditions, the /474 flow field is calculated by solving an unsteady boundary Laplace equation. A "point source function" method is used to convert the differential equation to integrals. The shape of the unknown boundary is repeatedly adjusted to reach the correct position. The particle trajectory is calculated by solving a series of regular differential equations. Based on the magnitude of S_t , either the perturbation method, Treanor method or R-K method can be used. Our computation shows that the impact points of the particles on the plate are primarily concentrated in the range $X < 2$. The calculation made for very large H is still valid at $H=1.5$. After taking the effect of viscosity which causes non-uniformity of the velocity at the jet outlet into account, a

velocity distribution $v_w/\bar{v}_w=1.264(1-2x/D)^{1/6}$ is used to correct the results. A $P(\bar{S}_t, \alpha^*)$ curve is obtained. A sampler was designed according to that curve and its performance met the design specifications^[7].

This work was completed under the guidance and assistance of Professor Wu Chenkang. Professor Ban Yinggui also provided guidance and assistance. Comrade Li Jiachun provided many valuable opinions on the manuscript. The author wishes to thank them for their efforts.

References

- [1] William Dicht, Air Pollution Control Engineering, Chap. 3, 5, Marcel Dekker, Inc., New York and Basel, 1980.
- [2] Schach, W., Umlenkung eines kneisforinigen Flussigkeitssstrahles an einer ebenen Platt senkrecht znr Stromungsrichtung, ZAMP 6 (1935) S51-59.
- [3] Treanor, C.E., A Method for the Numerical Integration of Coupled First Order Differential Equation with Great Different Time Constants, Math. of Computation, 20, 93 (1966), 39-45.
- [4] Schlichting, H., Boundary-Layer Theory, sixth Edition, 91-92, 174-175, 689-690.
- [5] Marple, V.A. et al., Inertia Impactors, in Benjamin Y.H. Liu ed., Fine Particles, 411, Academia Press, Inc., New York San Francisco London, (1976).

- [6] Wiedemann, R., Measurement of Particle Size Distributions of Flue Dust by Means of Cascade Impactors, in Michel M. Benarie ed., Atmospheric Pollution (1980), 257, Elsevier Scientific Publishing Company Amsterdam-Oxford-New York, (1980).
- [7] Liu Dayou, Multi-stage Impact Sampler for Atmospheric Particles, Journal of Environmental Science, 3, 4 (1983), 319.

CALCULATION OF THE CIRCULAR JET WITH PARTICLES IMPACTING UPON A PLATE

Liu Dayou

(Institute of Mechanics, Academia Sinica)

Abstract

The calculation of the flow field of a uniform circular jet with particles impacting upon an infinite plate perpendicularly is presented. The fluid is assumed to be inviscid and incompressible. The trajectories of small spherical particles carried in the jet are also calculated by choosing either $\frac{24}{Re}$ or $\frac{24}{Re} (1 + Re^{1/2})$ as drag coefficient.

Assuming that the particles are uniformly distributed initially in the jet, we obtain the curves of impact efficiency (known as collection probability in the study of samplers). The basis upon which the assumptions are made in the calculation is discussed. Viscous effects are analyzed, and then some corrections of the curves $P(S, \Omega^*)$ considering these effects are made. The results of calculation show that the impact points of the particles on the plate mainly concentrate in the zone of $x < 2$. The results of calculations based on very large H is valid for $H > 1.5$. An appraisal for the sampler designed by using $P(S, \Omega^*)$ curves shows that expected performance has been realized.

Distribution Near a Cracked Tip

Yu Jilin (University of Science and Technology of China)
and Zheng Zhemin (Institute of Mechanics, Academia Sinica)

Abstract

A non-local elastic plastic continuum model is presented. In this model, the relation between stress and elastic strain is non-linear and plastic strain is related to the history of total strain. With regard to the deformation theory, it is assumed that the plastic strain tensor is proportional to the total strain deviation tensor. The proportionality factor is a scalar function of the total effective strain. This model was used to analyze the stress field at the tip of a power-law hardening material with a tensile crack. Based on the results of RR asymptotic solution of the tensile cracked tip obtained in classical fluid dynamics, expressions for the distribution of tensile stress in front of the crack and the maximum tensile stress were derived through one-dimensional simplification. They showed that the J integral criterion might be obtained from the maximum tensile stress criterion. Existing experimental data were used to calculate the maximum stress near the tip of several steel materials as the crack begins to propagate. It was discovered that its order of magnitude is close to that of the cohesive strength of the lattice. The results obtained are useful for the understanding of the physical mechanism of the fracture process of the material.

I. Introduction

In the recent two decades, based on classical elastic mechanics and elastic plastic mechanics, fracture mechanics has been developed at a rapid pace. It serves as a new theoretical basis for the safety design of engineering components, estimation of useful life and evaluation of the performance of engineering materials. It is very successful in engineering applications.

Classical fracture mechanics was developed based on the equilibrium criterion which was proposed by Griffith and extended by Orowan. The concept of J integral is also based on energy analysis. This type of energy criterion avoids the physical mechanism of the fracture process, i.e., the stress and strain conditions near the cracked tip. In reality, according to classical continuum mechanics, there is a stress singularity at the tip. The widely used concept of stress strength factor and the HRR analysis of power-law hardening materials recognize this singularity. However, if this singularity exists, the cracked body cannot sustain any load. This contradiction is one of the major deficiencies of classical fracture mechanics.

Many attempts were made to eliminate such stress singularity, including the linear yield band model of Dugdal^[1], radius of curvature correction made by Neuber^[2], dislocation model of Bilby et al^[3] and super dislocation model of Atkinson et al^[4]. These models mostly involve local correction on the basis of classical theory. They are useful for certain practical problems. However, the physical basis is ambiguous.

Some people^[5,6] believe that there is always a radius of curvature at the tip crack. The ideal sharp crack does not exist. Microscopically (on the order of μm), it may be the case. However, the fracture process is essentially the destruction of the atomic bond. On a finer scale, plasticity does not flow uniformly. There are dislocation cells when the strain level is high. There is a theory^[7] which proves that in most metals, with the exception of face-centered metals and alkali metals, the sharp crack on the atomic scale will not become dull. Iron is in the middle. Therefore, despite the possible plastic deformation near the tip, the crack

Manuscript received on January 16, 1984.

may still remain sharp when the accuracy is on the atomic scale./486

In reality, a material is composed of discrete atoms. It has a complex internal structure. Physical quantities corresponding to the continuum field, such as displacement, strain, stress, etc., can only be established on the basis of local averages. When the characteristic scale of the physical phenomenon under consideration is comparable to that of the internal structure of the material, classical continuum mechanics will encounter difficulties. A more rational physical structure theory must take the internal structure of the material into account. To this end, since the 60's, various continuum theories which take the micro-structure of the material in consideration were developed. In treating problems relating to cracked tip and its stress singularity, the non-local theory developed by Eringen

et al^[8,9] has been successfully applied.

The non-local theory considers that the interaction between atoms is a long range force. Therefore, the stress on a point is not only related to the strain and strain history at that point, but also related to the strain and strain history at other points in the object. In other words, the stress at a point is a general function of the strain field of the entire object and its history.

Eringen and his colleagues used the non-local theory to study the stress field at the tip of a brittle single crystal material. Their results showed that the stress singularity at the cracked tip did not exist. The maximum stress appeared at a small distance in front of the cracked tip. In addition, the theoretical cohesive stress determined is in agreement with those obtained by using atomic theory and by experimental prediction^[10]. This means that the cracked body also meets the maximum stress fracture criterion. Based on the non-local elastic theory, it is not necessary to introduce the surface energy which has no clear physical significance in classical theory to directly derive the Griffith criterion from the maximum stress criterion. Therefore, the physical significance of the finding is very high.

In this work, the non-local theory is used to study the cracking problem in elastic plastic materials. When plastic deformation is involved, the state of stress is related to the strain history. Let us consider a metallic lattice (single crystalline or polycrystalline). Under an external load, if there is only elastic deformation, the spacing between neighboring atoms in the material deviates only very slightly

relative to its equilibrium value. Once the external load is removed, these atoms can still return to their original states. However, plastic flow is related to the motion and increase of dislocations in the crystalline material. In other words, the plastic deformation of material signifies permanent changes of the atomic arrangement, i.e., relative positions of atoms, in the material. As a plastic flow develops, there is a new equilibrium in every instance. Due to the presence of the external load, there is a small deviation of the atomic spacing away from the new equilibrium state. Based on this physical picture, stress is corresponding to the deviation of atomic spacing away from the equilibrium state at that instance, i.e., the elastic portion of strain. Considering the fact that the interaction between atoms is a long range force, stress and elastic strain should be described by a non-local relationship. However, plastic strain corresponds to the permanent change of equilibrium atomic arrangement. It should be related to the total strain history. Based on the small deformation theory and plastic deformation theory, the structure and basic equations for this type of power-law hardening non-local elastic plastic material were established in this work. Furthermore, it was used to study the stress field near the tip with a tensile crack. The HRR singularity solution of a tensile crack near the tip obtained by classical fracture mechanics was used to derive the expression for the maximum stress near the tip in small scale yield under one-dimensional simplification. It has been proven that the critical J integral criterion in classical fracture mechanics can be obtained from

the maximum stress criterion on the non-local elastic plastic theory. Existing experimental data were used to calculate the critical maximum stress values near the cracked tips of several steel materials. It was discovered that it is of the same order of magnitude as the internal cohesive stress of the lattice. Finally, the physical meanings of this theory and its results are discussed.

II. Basic Equations

In this work, the plastic structure is described in the strain space because, as described in the previous section, that plastic deformation is related to the total strain, rather than stress.

According to the small strain theory, strain ϵ is related to displacement u linearly, i.e.

$$\epsilon_{ij} = 1/2 (u_{i,j} + u_{j,i}) \quad (1) \quad /487$$

where the subscript following the comma represents the partial derivative with respect to the corresponding coordinate.

The strain is divided into two parts, i.e. elastic strain and plastic strain:

$$\epsilon_{ij} = \epsilon_{ij}^e + \epsilon_{ij}^p \quad (2)$$

where the superscripts e and p represent elastic and plastic, respectively. Let us assume that elastic strain ϵ^e and stress t satisfy a non-local linear relation [8]

$$t_{ij}(x) = \int_V [\lambda'(|x'-x|) \epsilon_{kk}^e(x') \delta_{ij} + 2\mu'(|x'-x|) \epsilon_{ij}^e(x')] dV(x') \quad (3)$$

where δ_{ij} is Kronecher's δ , and λ' and μ' are non-local modulus.

All repeating subscripts indicate the summation with respect to

all indices. Let us assume that the effect of factors such as the internal characteristic scale change of the materials and microscopic inhomogeneity due to plastic deformation on non-local modulus can be neglected. Then, λ' and μ' is only a function of position $|x'-x|$.

When there is no volumetric force, the stress equilibrium equation is

$$t_{ij,j} = 0 \quad (4)$$

In order to discuss the plastic structure, we introduced strain deviation e and elastic strain deviation e^e

$$e_{ij} = \epsilon_{ij} - \frac{1}{3} \epsilon_{kk} \delta_{ij}, \quad e^e_{ij} = \epsilon^e_{ij} - \frac{1}{3} \epsilon^e_{kk} \delta_{ij} \quad (5)$$

as well as effective strain $\bar{\epsilon}$ and effective elastic strain $\bar{\epsilon}^e$

$$\bar{\epsilon} = \sqrt{\frac{2}{3} e_{ij} e_{ij}}, \quad \bar{\epsilon}^e = \sqrt{\frac{2}{3} e^e_{ij} e^e_{ij}} \quad (6)$$

Corresponding to the classical plastic deformation (full) theory, in the strain space we assume that:

1. The volumetric strain is elastic, i.e., $\epsilon^p_{kk} = 0$. Plastic strain is only related to the deviation of total strain.
2. The effective elastic strain is a well-defined function of the effective total strain.
3. The plastic strain tensor is proportional to the total strain deviation tensor. The proportionality constant is the scalar function of the total strain, i.e.

$$\epsilon^p_{ij} = \varphi(\bar{\epsilon}) e_{ij} \quad (7)$$

A nominal local stress σ is introduced. It is related to elastic strain and the classical generalized Hooke law:

$$\sigma_{ij} = \lambda \epsilon_{kk}^e \delta_{ij} + 2\mu \epsilon_{ij}^e \quad (8)$$

where λ and μ are Lamé constants. The effective nominal local stress is defined as

$$\bar{\sigma} = \sqrt{\frac{3}{2} s_{ij} s_{ij}} \quad (9)$$

where

$$s_{ij} = \sigma_{ij} - \frac{1}{3} \sigma_{kk} \delta_{ij} \quad (10)$$

is the deviation of σ .

Let us consider a uniform deformed body. Obviously, in this case the nominal local stress σ is equal to the non-local stress (true stress) t . Therefore, the $\bar{\sigma}$ - $\bar{\epsilon}$ curve is the same as the stress-strain curve in the event of a simple tensile stress for an incompressible material. For a power-law hardening material, we have

$$\bar{\sigma} = \begin{cases} \sigma_y (\bar{\epsilon}/\epsilon_y) & \text{when } \bar{\epsilon} \leq \epsilon_y \\ \sigma_y (\bar{\epsilon}/\epsilon_y)^n & \text{when } \bar{\epsilon} > \epsilon_y \end{cases} \quad (11) \quad /488$$

where n is the strain hardening index. σ_y and ϵ_y are the yield stress and strain in simple tensile situations. Notice that when $s_{ij} = 2\mu \epsilon_{ij}^e$ the above formula can be converted into a relation between $\bar{\epsilon}$ and $\bar{\epsilon}^e$.

$$\frac{\bar{\epsilon}^e}{\epsilon_y} = \begin{cases} \bar{\epsilon}/\epsilon_y & \text{when } \bar{\epsilon} \leq \epsilon_y \\ (\bar{\epsilon}/\epsilon_y)^n & \text{when } \bar{\epsilon} > \epsilon_y \end{cases} \quad (12)$$

Based on assumption (2) above, this relation is still valid for a non-uniform deformation (in this case $t_{ij} \neq \sigma_{ij}$). From equations (7) and (12) we can solve that

$$\varphi = \begin{cases} 0 & \text{when } \bar{\epsilon} \leq \epsilon_y \\ 1 - (\bar{\epsilon}/\epsilon_y)^{n-1} & \text{when } \bar{\epsilon} > \epsilon_y \end{cases} \quad (13)$$

Thus, equations (1)-(7) and (13) form the basic equations in the non-local elastic-plastic deformation theory of power-law hardening materials which are incompressible and are deformed slightly. It is only applicable to simple loading and near simple loading situations.

III. Stress Field Near the Tip of a Tensile Crack Under Plane Strain

Let us assume that there is a crack, $2a$ in length, on an infinite plate. The surface is free. At infinity, there is a uniform tensile stress t_∞ perpendicular to the crack plane (see Figure 1). Near the cracked tip, plastic strain is much larger than elastic strain. Therefore, the incompressibility assumption is approximately valid. If we are limited to the study of the initial propagation of a crack, deformation theory is also applicable to power-law hardening materials. When the dimension of the plastic region is smaller than the thickness of the plate, it can be approximately considered as in a plane strain state. Because of symmetry, we are only required to study the upper plane.

$$\left. \begin{aligned} s_{ii} &= \frac{1}{2} (u_{i,i} + u_{i,i}), \quad s_{ii,i} = 0, \quad s_{ij} = s_{ij}^e + s_{ij}^p \\ s_{ij} &= \int_0^{\infty} [\lambda'(|x' - x|) s_{ij}^e(x') \delta_{ij} + 2\mu'(|x' - x|) s_{ij}^p(x')] ds(x') \\ s_{ij}^p &= \begin{cases} 0 \\ \left[1 - \left(\frac{s}{s_0}\right)^{n-1}\right] \left(s_{ij} - \frac{1}{3} s_{kk} \delta_{ij}\right) \end{cases} \end{aligned} \right\} \quad (14)$$

The problem is reduced to solving the equations in two-dimensions under the following boundary conditions:

$$\left. \begin{aligned} t_{11} &= t_{12} = 0, \quad t_{22} = t_{\infty}, \quad \text{when } (x_1^2 + x_2^2) \rightarrow \infty \\ t_{12} &= t_{22} = 0, \quad \text{when } x_2 = 0, \quad |x_1| < a \\ \partial u_1 / \partial x_2 &= 0, \quad u_2 = 0, \quad \text{when } x_2 = 0, \quad |x_1| \geq a \end{aligned} \right\} \quad (15)$$

The last condition is obtained from symmetry.

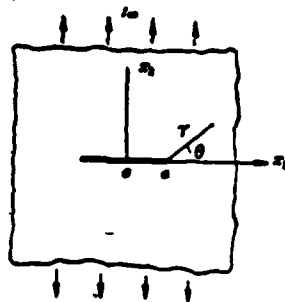


Figure 1. The Tensile Crack Problem

Eringen^[8] proved that the non-local modulus can be expressed as

$$\lambda' = \lambda \alpha(|x' - x|), \quad \mu' = \mu \alpha(|x' - x|) \quad (16)$$

where $\alpha(|x'-x|)$ is a non-negative function of x' which has the following properties:

1. With increasing $|x'-x|$, $\alpha(|x'-x|)$ approaches zero very rapidly.
2. In the extremum case in classical elastic theory, $\alpha(|x'-x|)$ becomes a Dirac δ function.
3. $\int_V \alpha(|x'-x|) dV(x') = 1$.

By comparing to the ideal lattice model, we get

$$\alpha(|x'-x|) = \begin{cases} K(1 - \frac{|x'-x|}{b}) & |x'-x| \leq b \\ 0 & |x'-x| > b \end{cases} \quad (17)$$

where b is the lattice parameter and $K=3/\pi b_2$ (two-dimensional) or $K=1/b$ (one-dimensional).

Based on equation (16), the equilibrium equation (4) can be rewritten as

$$\int_V \alpha(|x'-x|) \sigma_{ij}(x') dV(x') = 0 \quad (18)$$

It can be proven that if the effect of surface tension can be neglected the necessary and sufficient condition for the above equation to be satisfied is:

$$\sigma_{ij,j} = 0 \quad (19)$$

This shows that the control equation for the nominal non-local stress is the same as that in classical theory. Thus, if the effect of surface tension is neglected, for a given displacement and boundary condition, the displacement field and strain field obtained using the model described in this paper are identical to those obtained based on the classical elastic plastic theory. However, the stress field must be calculated using equation (14).

The above conclusions is generally not valid for problems with given stress boundary conditions or mixed boundary conditions. If classical strain field is used to calculate the non-local stress field, stress boundary conditions can only be approximately satisfied. Despite so, because the microscopic scale reflecting the non-local effect is very small (atomic spacing), actual errors only occur at places where classical theoretical stress has breakdowns or irregularities (of course, those are the areas of concern). The calculations performed by Eringen^[9] on a non-local elastic crack showed that this error decreased with increasing $2a/b$. When $2a/b=40$ (equivalent to a crack length around $0.1\mu\text{m}$), the maximum stress error is about 10%. The actual crack is much larger. The error will be less.

For power-law hardening materials, based on classical theory of elastic plastic deformation, the stress and strain at the tip have $r^{-n/1+n}$ and $r^{-1/1+n}$ singularities, respectively. According to reference [12], in small range yield cases, the major terms of stress and strain fields near the tip can be expressed as:

$$\left. \begin{aligned} \sigma_{rr} &= \left[\frac{(1-\nu^2)\pi a r_0^2}{l_0 r \sigma_y^2} \right]^{\frac{2}{1+n}} \sigma_y \bar{\sigma}_{rr}(\theta) \\ \sigma_{\theta\theta} &= \left[\frac{(1-\nu^2)\pi a r_0^2}{l_0 r \sigma_y^2} \right]^{\frac{2}{1+n}} \sigma_y \bar{\sigma}_{\theta\theta}(\theta) \\ \sigma_{r\theta} &= \left[\frac{(1-\nu^2)\pi a r_0^2}{l_0 r \sigma_y^2} \right]^{\frac{2}{1+n}} \sigma_y \bar{\sigma}_{r\theta}(\theta) \\ \epsilon_{rr} &= \left[\frac{(1-\nu^2)\pi a r_0^2}{l_0 r \sigma_y^2} \right]^{\frac{1}{1+n}} \epsilon_y \bar{\epsilon}_{rr}(\theta) \end{aligned} \right\} \quad (20)$$

$$\left. \begin{aligned} \epsilon_{\theta\theta} &= \left[\frac{(1-\nu^2)\pi\sigma_0^2}{I_n r \sigma_0^2} \right]^{\frac{1}{1+n}} \epsilon_{\theta\theta}(\theta) \\ \epsilon_{r\theta} &= \left[\frac{(1-\nu^2)\pi\sigma_0^2}{I_n r \sigma_0^2} \right]^{\frac{1}{1+n}} \epsilon_{r\theta}(\theta) \end{aligned} \right\} \quad (21)$$

where ν is the elastic Poisson's ratio of the material and I_n is a constant related to the hardening index n (see Figure 2). $\sigma_{rr}(\theta), \dots, \epsilon_{r\theta}(\theta)$ are angular distribution functions corresponding to $\sigma_{rr}, \dots, \epsilon_{r\theta}$ which are also related to n . The angular distribution functions of three stress values at different n are shown in Figure 3.

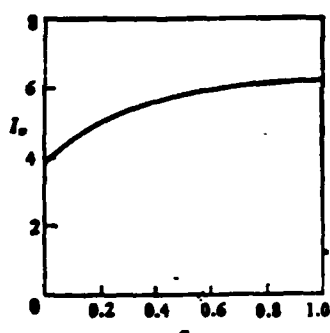


Figure 2. I_n vs. n

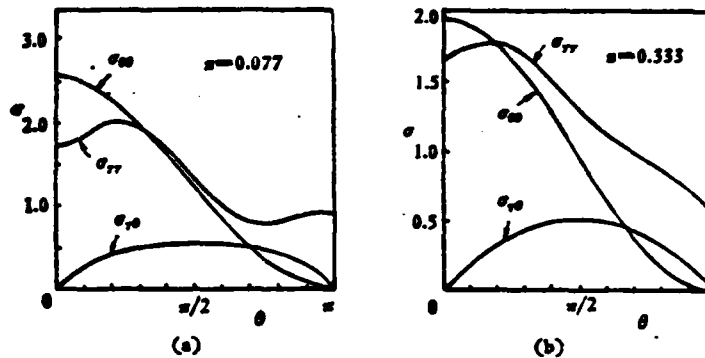


Figure 3.- Stress vs. θ at Various Hardening Indices (from reference [12])

If equation (21) can also be considered as an acceptable approximate solution of the strain field in non-local elastic plastic theory, based on equation (20) we can find the approximate solution of the non-local stress field from the following equation:

$$\sigma_{ij} = \int_V \alpha(|\mathbf{x}' - \mathbf{x}|) \sigma_{ij}(\mathbf{x}') dV(\mathbf{x}') \quad (22)$$

This is a very difficult task which will not be investigated further in this paper. One can see that t_{ij} is bound and stress singularity no longer exists at the tip.

IV. One-dimensional Approximate Analysis of Non-local Tensile Stress in Front of Crack

In order to obtain a clear qualitative physical picture of the non-local stress field at the tip, in this section we will

attempt to simplify the equation to one-dimension, i.e., to use the following

$$\epsilon(x) = \int_{x-b}^{x+a} \frac{1}{b} \left(1 - \frac{|x' - x|}{b}\right) \sigma(x') dx' \quad (23)$$

to calculate the tensile stress in front of the crack (for convenience, subscripts are omitted). This is equivalent to assuming that the stress along x_2 -direction remains unchanged at least in the atomic scale and non-local action is only active along the crack.

From equations (20) and (23) it is easy to find

$$\begin{aligned} & 0 && \text{when } 0 \leq x < a-b \\ & \left| \frac{(1+n)^2}{2+n} \left(\frac{x-a}{b} + 1 \right)^{\frac{1+n}{1+n}} \right| \sigma_0 && \text{when } a-b \leq x < a \\ & \epsilon(x) = \left| \frac{(1+n)^2}{2+n} \left[\left(\frac{x-a}{b} + 1 \right)^{\frac{1+n}{1+n}} - 2 \left(\frac{x-a}{b} \right)^{\frac{1+n}{1+n}} \right] \right| \sigma_0 && \text{when } a \leq x < a+b \quad (24) \\ & \left| \frac{(1+n)^2}{2+n} \left[\left(\frac{x-a}{b} + 1 \right)^{\frac{1+n}{1+n}} - 2 \left(\frac{x-a}{b} \right)^{\frac{1+n}{1+n}} + \left(\frac{x-a}{b} - 1 \right)^{\frac{1+n}{1+n}} \right] \right| \sigma_0 && \text{when } x \geq a+b \end{aligned}$$

/491

where

$$\sigma_0 = \left[\frac{(1-n^2) \pi a r_0^2}{l_0 b \sigma_f^2} \right]^{\frac{2}{1+n}} \sigma_f \delta_{ss}(0).$$

Figures 4 and 5 show the tensile stress distribution with different internal structure scales.

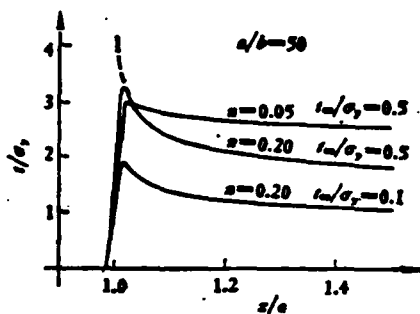


Figure 4. Tensile Stress Distribution in Front of Crack when $a/b=50$. Dotted line represents the classical solution when $n=0.2$, $t_{\infty}/\sigma_y=0.5$.

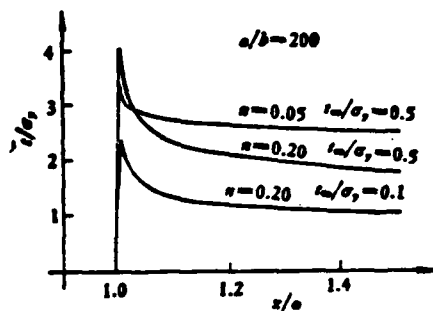


Figure 5. Tensile Stress Distribution in Front of Crack when $a/b=200$.

It is obvious that as long as b is not zero, the stress in front of the crack is always finite. The maximum stress occurs at $r=b/2^{1+n}-1$. It is

$$i_{\max} = A_n \left[\frac{(1-\nu^2) \pi a i_0^2}{b \sigma_y} \right]^{\frac{n}{1+n}} \sigma_y \quad (25)$$

where

$$A_n = \frac{(1+n)^2 \bar{\sigma}_{90}(0)}{\left(1 + \frac{n}{2}\right) I_n^{\frac{n}{1+n}} (2^{1+n} - 1)^{\frac{1}{1+n}}} \approx \frac{0.91}{n + 0.31}$$

is a constant related to the hardening index, as shown in Figure 6. Based on this, the stress concentration factor is

$$P = \frac{i_{\max}}{i_0} = A_n \left[(1-\nu^2) \pi \frac{a}{b} \right]^{\frac{n}{1+n}} \left(\frac{i_0}{\sigma_y} \right)^{-\frac{1-n}{1+n}} \quad (26)$$

It is not only related to the relative scale of crack to internal structure, but also to the hardening index as well as to the relative magnitude of external load to yield stress. This is an apparent result due to non-linearity of plasticity.

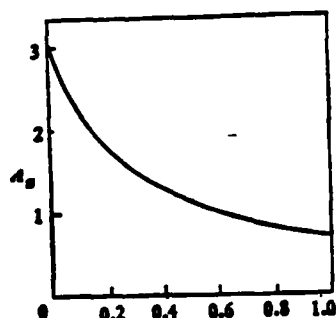


Figure 6. Coefficient A_n vs. Hardening Index n .

Since the stress near the tip is finite, naturally we can establish a physical criterion for cracking: there is a critical stress t_c , which is a constant for a material, when $t_{\max} = t_c$, crack will begin to propagate.

Equation (25) can also be written as

$$t_{\max} = A_n \sigma_y \left(\frac{1/E}{b} \right)^{\frac{n}{1+n}} \quad (27)$$

where E is the Young's modulus. Because n , A_n , b , σ_y , and E are material constants, therefore, the criterion in classical /492 elastic-plastic fracture mechanics can be directly obtained based on this fracture criterion. Thus, the contradiction in classical fracture mechanics as pointed out in the introduction can be bypassed. The macroscopic model of fracture mechanics is unified with the microscopic physical mechanism.

It is worthwhile to note the physical significance of critical stress t_c . The quasi-embrittlement fracture and ductile fracture of alloys are far more complicated than the fracture of a single crystal. On one hand, because of the presence of intergranular boundary, alloying elements and various metallographic structures, the microscopic structure is non-uniform. On the other hand, as plastic deformation progresses, the microscopic structure also continues to change. Despite so, we can still anticipate that the critical stress t_c corresponds to the case that the cohesive strength between atoms at the leading edge of the crack has the same order of magnitude as the cohesive strength of the lattice of the base metal (which is

around $0.1E$ for most metals) after undergoing a severe plastic deformation. Table 1 shows the t_c/E values for several steel materials calculated from available experimental data. The results are in good agreement with the above analysis. From the data one can see that although materials of similar composition may have large variations in yield strength σ_y , yet their t_c values are relatively stable when the fracture mode is identical. The numerical value is slightly less than the cohesive strength of a perfect lattice. This reduction is not surprising if we consider factors such as local stress concentration due to a large number of lattice defects and dislocations near the tip prior to failure. Obviously, the microscopic structure of the material is different due to various heat treatment conditions. Therefore, the effect of the above factors is also different. Thus, the value of t_c varies slightly. In Table 1, the data on two Fe-20% Co-15% Cr-5%Mo alloys reflect this variation. The data are arranged in descending order based on effective time. As it increases, the residue Austenite content decreases and the precipitate phase increases. Thus, the atomic binding force decreases and the local stress concentration effect is strengthened. t_c will decrease slightly.

Table 1. Ratio of Critical Stress Calculated Based on Experimental Data to Young's Modulus for Several Materials

1. 钢 种	σ_s (MN/m ²)	σ	J_s (MN/m)	σ_s/E	数据来源 2.
GCr 15	636	0.17	0.086	0.093	[13]
	451	0.21	0.046	0.104	
	411	0.21	0.030	0.091	
34 CrNiMo	1225	0.10	0.032	0.060	[6]
	1450	0.085	0.038	0.059	
30SiMnCrMo	980	0.12	0.119	0.073	[6]
	1156	0.11	0.117	0.073	[14]
	1156	0.10	0.119	0.064	
Fe-20%Co-15%Cr-5%Mo 3. (高纯)	1390	0.066	0.0413	0.046	[15]
	1580	0.058	0.0247	0.045	
	1750	0.051	0.0203	0.045	
	2110	0.034	0.0057	0.042	
	2300	0.021	0.0018	0.040	
Fe-20%Co-15%Cr-5%Mo 4. (高纯、脱氧)	1590	0.076	0.0436	0.058	[15]
	1810	0.070	0.0215	0.058	
	2140	0.050	0.0051	0.050	
	2360	0.033	0.0018	0.045	

1. type of steel
2. source of data
3. high purity
4. high purity, de-oxygenated

V. Discussion and Conclusions

1. In spite of the fact that the structure is only given based on plastic deformation in this paper, this basic concept is also applicable to other types of plastic structure relations. Regardless which structural assumption is adopted, we must use strain space to describe the problem. In this space, the

classical stress vs. elastic strain relation can be used to transform stress into elastic strain. This type of treatment also ensures that the present model is consistent with the classical model when the internal scale in the non-local modulus approaches zero.

2. Different from the non-local plastic theory recently introduced by Eringen^[16], this model (does not take the non-local characteristic of the plastic structure into account. This is because the physical characteristic scale relating to plastic deformation is far larger than the characteristic scale considered in non-local elasticity (atomic scale). Relative to atomic scale, plastic deformation is highly non-uniform. From another angle one can say that the plastic deformation of a point is somewhat random in nature. Hence, when the accuracy is on the atomic scale we should understand that the continuity of plastic strain is described as the statistical average of all probable deformations in the neighborhood of the point under investigation. The physical connection between plastic strain and stress, however, is expressed as the internal stress caused by the growth of dislocations. Statistically, it is equal to zero. Therefore, macroscopically plastic strain is not directly related to stress. However, microscopically, this internal stress causes the average cohesive strength to drop. Mathematically, the model introduced in this work decouples the non-local (elastic) and non-linear (plastic) parts of the basic equations. Consequently, it is more convenient to use in

practical problems.

3. Strictly speaking, in the fracture region near the tip, geometrical non-linearity caused by a large strain cannot be neglected. J integral is only applicable outside this region. Thus, if the entire region is treated based on the small strain linear theory, it will lead to some error. Despite so, the non-local elastic plastic theory recommended in this work can unify the macroscopic model of fracture mechanics with the microscopic physical mechanism. Furthermore, the critical fracture stress thus obtained is on the same order of magnitude as the cohesive stress of the lattice. This will benefit the understanding of the physical mechanism of the material fracture process.

4. In metal physics, the effect of microstructure factors such as two-phase particle volume fraction, particle size and impurity spacing on the fracture resistance is discussed in detail. In the present model, these factors affect the fracture resistance of materials through σ_y and n , i.e., the change of plastic deformation in front of the crack.

5. The fracture of a metal involves three different scales: macroscopic, fine detail and microscopic. In this work, an attempt was made to connect microscopic and macroscopic viewpoints. From the fine details, many physical factors are yet to be considered. It is necessary to understand the dependence of internal cohesive stress upon fine factors such as alloy composition, metallograph and microscopic structure as well as upon macroscopic parameters such as hardening index and

destructive strain which describe the extent of plastic deformation. A great deal of detailed theoretical and experimental work is required.

References

- [1] Dugdale, D.S., J. Mech. Phys. Solids, 8, 2(1960), 100-104.
- [2] Neuber, H.Z., Kerbspannungslehre, (1937), Concentration of Stress, translated by Dhao Xusheng (1958).
- [3] Bilby, B.A., Cottrell, A.H. and Swinden, K.H., Proc. Roy. Soc. London, A272 (1963), 304-314.
- [4] Atkinson, C. and Kay, T.R., Acta Metallurgica, 19, 7(1971), 679-683.
- [5] Rice, J.R. and Johnson, M.A., Inelastic Behavior of Solids ed. M.F. Kanninen et al, (1970), 641-670.
- [6] Chen Hu, Collection of Metal Fracture Studies, Chen Hu et al, (1978), 135-156.
- [7] Rice, J.R. and Thomson, R., Philosophical Magazine, 29 (1974), 73-97.
- [8] Eringen, A.C., Continuum Mechanics Aspects of Geodynamics and Rock Fracture Mechanics, ed. P.T. Christensen (1974), 494 81-105.
- [9] Eringen, A.C., Spezial, C.G., and Kim, B.S., J. Mech. Phys. Solids, 25 (1977), 339-355.
- [10] Eringen, A.C., Crystal Lattice Defects, 7 (1977), 109-130.
- [11] Eringen, A.C., J. Phys. D: Appl. Phys., 10 (1977), 671-678.
- [12] Hutchinson, J.W., J. Mech. Phys. Solids, 16, 1(1968), 13-31.

- [13] Hong, Y., Yeh, Y. and Xia, X., Mechanical Behavior of Materials-IV (ICM4), ed. J. Carlsson et al. 2 (1983), 849-855.
- [14] Chen Hu et al, Collection of Metal Fracture Studies, Chen Hu et al (1978), 92-108.
- [15] Musiol, C. and Brook, R., Eng. Fract. Mech., 9 (1977), 379-387.
- [16] Eringen, A.C., Int. J. Eng. Sci., 19, 12(1981), 1461-1474.

A MODEL OF NONLOCAL ELASTIC-PLASTIC CONTINUUM APPLIED TO THE STRESS DISTRIBUTION NEAR A CRACK TIP

Yu Jilin

(University of Science and Technology of China)

Zheng Zhemin

(Institute of Mechanics, Academia Sinica)

Abstract

A model of nonlocal elastic-plastic continuum is proposed. The stress and the elastic strain are related by a nonlocal linear relation, and the plastic strain is dependent on the history of total strain. For plastic deformation theory, it is assumed that the plastic strain tensor is proportional to the total strain deviation tensor and the ratio is a scalar function of the effective total strain.

This model is used to analyse the stress field at the tip of a crack in a power-law hardening material under plane strain condition. Based on the results of HRR asymptotic solution in classical fracture mechanics, the distribution of tensile stress on the line directly ahead of a crack tip and the expression for maximum tensile stress are calculated under one-dimensional simplification. It is shown that the J_c criterion may be obtained from the maximum tensile stress criterion of the nonlocal theory. Available experimental data for steels are used to calculate the maximum tensile stress of fracture initiation at the crack tip, which is found to be close to the theoretical cohesive strength. The results obtained are useful for understanding the fracture process and mechanism of materials.

Study of Plane Stress with Elastic Plastic Mixed Mode Fracture /495

Xu Jilin, Xue Yinian and Han Jinhu

(Institute of Mechanics, Academia Sinica)

Abstract

In this work, the deformation field around the crack of a thin aluminum plate with center cracks of various angles of inclination under tensile load was measured using the direct laser speckle method and Moire's method. In addition, the relation between loading and crack propagation in the steady-state crack growth process was measured. Moreover, finite element analysis based on large elastic-plastic deformation equation was carried out to obtain the stress-strain distribution around the crack. Calculated results are found in good agreement with experimental data. Furthermore, the results were discussed.

I. Introduction

In a thin wall structure of a malleable material with a crack, before the crack began to propagate, the crack tip has already formed a large plastic region. After the crack is initiated, there is a steady-state growth process. If the linear elastic fracture theory is still applied, the load capability of the structure will be under-estimated. Therefore, there is a need to establish an elastic-plastic fracture theory to conduct this investigation. In recent years, progress has been made in the study of elastic-plastic mode I fracture theory. New methods

and parameters are constantly being introduced. In references [1,2], many authors used different fracture criteria to study the initiation, steady-state propagation and ductility instability over a wide range of yield conditions. In addition, experimental data and finite element numerical analysis were combined to calculate the stress-strain field near the crack tip. Furthermore, various fracture parameters were analyzed. Among them, Shih et al conducted a great deal of experimental work and numerical analysis under plane strain for large range yield. After sorting various fracture parameters, it was recommended that J_{1c} and δ_{1c} be used to express the initiation of a crack, and the tear modulus T_J and T_δ be used to express the growth of the crack. Kanninen believed that J and CTOA are the most effective parameters to estimate the initiation, steady-state growth and ductility instability of a malleable material. In the study of the plane stress fracture problem, Feddersen^[3] used aluminum alloy plates with center cracks to conduct a large number of experiments. A useful analytical method for engineering design was provided. However, the steady-state crack propagation process was only quantitatively described. We measured the relation between steady-state crack growth and load increment by using thin aluminum alloy plates with center cracks under tensile load^[4]. Moreover, based on the elastic plastic fracture model of plane stress--the shrink neck band model^[5], the elastic-plastic deformation finite element method was used to calculate the steady-state growth of Mode I crack^[6]. The calculated results and experimental data^[4] are in good

agreement. There is little published work on the study on mixed mode fracture for large range yield. Ueda et al^[7] studied the initiation of Mode I and Mode II cracks under large range yield conditions. They conducted some low temperature embrittlement tests with soft steel cross specimens with inclined cracks under the tensile stress in two axes. In the meantime, they conducted elastic-plastic finite element calculation for plane stress. They used the COD concept for Mode I fracture to analyze the initiation of a mixed mode crack.

In this work, thin aluminum alloy plates with center cracks at various angles of inclination under tensile load were used in the experimental study in plane stress conditions. Both the laser speckle method and Moire's used. In addition, the finite element method with elastic-plastic deformation was used to perform numerical analysis. The results were compared to experimental data and discussed.

II. Experimental

This experiment involves 20 specimens. They are thin plates with center cracks made of LY12-CZ and LY12-CS aluminum alloys.

Manuscript received on October 15, 1983. The paper was presented at the 1983 Beijing International Fracture Mechanics Academic Meeting.

The characteristic data of the materials are shown in Table 1. /496
These numbers were obtained in the tensile test of the raw materials. In the table, α and n are parameters in the expression $\epsilon = \sigma/E + \alpha[(\sigma/\sigma_{ys})^n - 1]$ in which an index curve is used

to approximate the curve of the material. The geometric dimensions of the specimen are shown in Figure 1. The angle of inclination between the crack line and the load $\beta=90^\circ, 60^\circ, 45^\circ$, and 30° . The initial crack length is $2a_0$. It ranges from 4.65mm to 42.7mm. Their projections in the direction perpendicular to the load range from 4.65mm to 23.8mm.

Table 1

表 1						
材 料	2. 弹性模量 $E(\text{kg/mm}^2)$	3. 屈服强度 $\sigma_y(\text{kg/mm}^2)$	4. 极限强度 $\sigma_b(\text{kg/mm}^2)$	5. 延伸率 δ_1	a	a
LY12-CZ	7100	32.5	45.5	0.184	0.01	8
LY12-CS	7100	32.5	45.2	0.143	0.0075	8

1. material
2. elastic modulus
3. yield strength
4. limiting strength
5. elongation

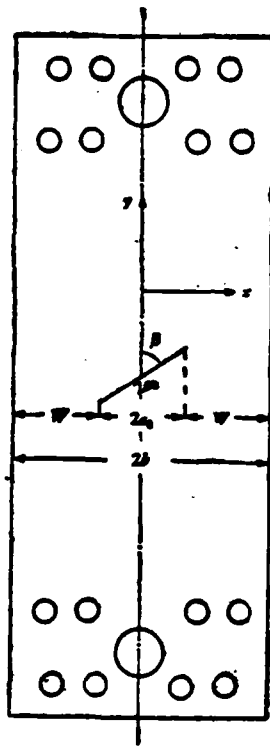


Figure 1

The center crack in the sample is cut by a 0.12mm diameter molybdenum and made into a fatigue crack. Fatigue cracks were not prepared on six specimens in order to study the effect of prepared fatigue crack on crack propagation.

Because the specimen is very thin, there is not much difference between surface and internal crack growth. In the experiment, an 80X microscope was used to read the crack growth increment Δa . The minimum scale on the microscope is 0.01mm.

The initiation and steady-state growth can be clearly observed through the microscope. The relation between load σ and crack growth ($a-a_0$) is thus determined.

In order to measure the strain distribution around the crack during the entire loading process, a laser speckle method is used to directly measure the deformation on one surface when the load is relatively low. On the other surface, Moire's method is used to determine the deformation when the load is relatively high^[8]. The surface on which the direct laser speckle method is used is polished by a wheel to improve the reflectivity of the surface in order to obtain high quality double exposure film for the analysis of the entire field. The analytical fringe pattern of the entire field is photographed through a 2mm diameter filter hole. The hole is opened up high to reach a sensitivity corresponding to a grating line density of 467 lines per millimeter. Hence, it is possible to measure the deformation field when the load is relatively low. When the load is relatively high, a simple Moire's method can be used to measure on the other surface even when deformation is large. The grating line density chosen is 40 lines per milliliter and the specimen grating is an orthogonal grating. The analyzing grating is a unidirectional grating of the same density. Based on the experimental data shown in Figure 8, the results of the speckle method and those of Moire's method are in good agreement:

In order to investigate whether the elastic-plastic Mode I fracture model of plane stress^[5] and crack growth criterion^[6]

can be extended to mixed mode fractures, we are concerned about the strain distribution on the ductile belt of the inclined center crack specimens (extension from the two apices of the crack along the direction perpendicular to the tensile direction is called the ductile belt). Moire's method was used to measure the strain ϵ_x in the x-direction and strain ϵ_y in the y-direction. Results show that ϵ_x is much smaller than ϵ_y .

III. Finite Element Analysis

/497

In this work, the Euler finite element formula with plane stress deformation was used to calculate and analyze aluminum alloy plates with center cracks under load at angles of inclination $\beta=60^\circ$, 45° and 30° to determine the stress σ_x , σ_y , τ_{xy} in the loading process, the stress σ_r , σ_θ and $\tau_{r\theta}$ around the crack top, the strain ϵ_x , ϵ_y , ϵ_z , γ_{xy} and the distribution of the plastic region. In addition, the open displacement of the crack surface and the strain ϵ_y on the ductile belt were calculated and compared to the experimental result (see Figures 8 and 9).

With regard to the steady-state crack growth on thin aluminum alloy plate specimens with center cracks at $\beta=90^\circ$, we had calculated the relation between crack growth and load increment, as well as the instability load, using the finite element method with plastic deformation equation based on the shrink neck band model of plane stress elastic-plastic fracture^[5]. The criterion of crack propagation was that the relative elongation of the shrink neck region at the crack tip reached the same level as the elongation coefficient of the material.^[6] The results are

in good agreement with the experimental data.

The speed equilibrium equation in the form of pseudo-work equation is

$$\int_V \left[\tau_{ij}^* \delta D_{ij} - \frac{1}{2} \sigma_{ij} \delta (2D_{ik}D_{kj} - v_{k,i}v_{k,i}) \right] dV \quad (1)$$

$$= \int_s f_i \delta v_i ds + \int_V b_i \delta v_i dV$$

where τ_{ij}^* is the Jaumann speed of Kirchhoff stress tensor τ_{ij} , σ_{ij} and D_{ij} represent the true stress tensor and deformation speed tensor, respectively. f_i and b_i are the instantaneous unit surface force and unit volume force. τ_{ij}^* and D_{ij} are related by the constitutive matrix of elastic deformation increment [C].

$$\{\tau^*\} = [C]\{D\} \quad (2)$$

From equation (1), we get the Euler finite element speed equilibrium equation

$$[K]\{\phi\} = \int_V [N]^T \{b\} dV + \int_s [N]^T \{f\} ds \quad (3)$$

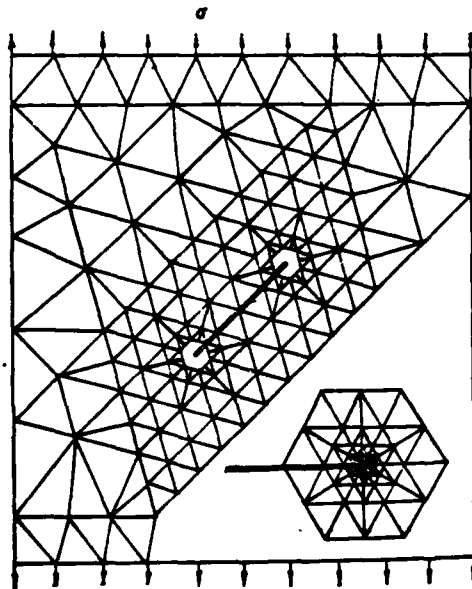


Figure 2

■ 2

$\{\dot{\phi}\}$ is the nodal point speed array. The rigidity matrix is /498

$$[K] = \int_V \{ [B]^T [C] [B] + [N_k]^T \sigma_{ij} [N_k]_{,i} - 2 [B_{ki}]^T \sigma_{ij} [B_{ki}] \} dV \quad (4)$$

In the plane stress case, let us assume that $\sigma_x = \sigma_{xx} = \sigma_{yz} = 0$. The instantaneous element thickness $t = t_0 e^{\epsilon_x}$.

When an increment tangent rigidity method is used to solve the problem, the load increment coefficient is determined by using the "Shantian" method to allow each element to enter a yield state in order to reduce the error introduced due to the discontinuity of the tangential modulus of the curve of the material at the elastic-plastic turning point. Moreover, it corrects for an unbalanced load.

The unit mesh for an inclined, center-cracked specimen is shown in Figure 2. The center-cracked unit lattice whose ratio of unit dimension at the crack tip to the crack length is

$$1/40 - 1/100, \beta = 90$$

is shown in reference [6].

IV. Results and Discussion

1. Fracture Surface Topography

From the fracture surfaces of all failed specimens one can see that there is a very small triangular flat cross-section in the neighborhood of the tip. It is rapidly turned into a 45° shear fracture with respect to the surface. It belongs to a plane stress fracture.

2. Fracture Stress

Table 2 shows the non-dimensional experimental data including the uniform tensile stress σ_1 and average stress

$\sigma_{i(\text{net})}$ on the ductile belt at initiation and the uniform tensile stress σ_c and average stress $\sigma_{c(\text{net})}$ on the ductile belt during unstable growth. These results show that the average stress on the ductile belt prior to the unstable growth of the crack has exceeded the yield of the material. Therefore, they most failed under the condition of large range yield.

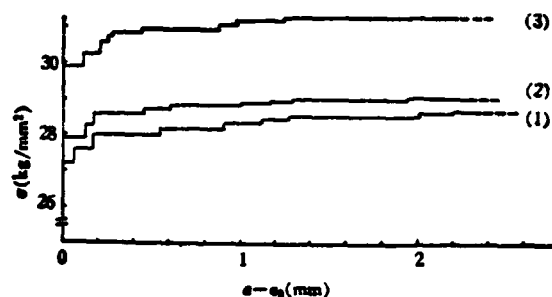


Figure 3a

- (1) specimen 28
- (2) specimen 24
- (3) specimen 19



Figure 3b

- (1) specimen 7

Table 2

表 2

试件号 ³	β	s (mm)	$2a_0$ (mm)	$\overline{2a_0}$ (mm)	$\frac{W}{b}$	$\frac{\sigma_i}{\sigma_{ys}}$	$\frac{\sigma_c}{\sigma_{ys}}$	$\frac{\sigma_i(\overline{W})}{\sigma_{ys}}$ ⁴	$\frac{\sigma_c(\overline{W})}{\sigma_{ys}}$ ⁵	$\frac{\sigma_c}{\sigma_u}$
1	90°	0.45	11.79	11.79	0.891	0.914	0.972	1.025	1.129	1.063
2			12.36	12.36	0.885	0.855	0.945	0.963	1.092	1.105
3			12.62	12.62	0.883	0.809	0.945	0.917	1.095	1.168
4 ¹⁾			11.05	11.05	0.898	0.963	0.982	1.077		1.020
5		0.89	4.65	4.65	0.957	1.071	1.095	1.117	1.175	1.022
6			5.81	5.81	0.946	1.031	1.086	1.092	1.175	1.053
7			11.55	11.55	0.893	0.899	1.003	1.009	1.166	1.116
8			18.30	18.30	0.830	0.720	0.889	0.868	1.132	1.235
9			23.78	23.78	0.780	0.720	0.831	0.926	1.111	1.154
10 ¹⁾		1.50	10.10	10.10	0.906	0.939	0.954	1.034		1.016
11 ¹⁾	13.46		13.46	0.878	0.942	0.991	1.074	1.182	1.052	
12 ¹⁾	14.47		14.47	0.868	0.935	0.985	1.077	1.191	1.053	
13 ¹⁾	21.68		21.68	0.803	0.735	0.825	0.914	1.062	1.122	
14 ¹⁾	10.05		10.05	0.909	0.985	0.997	1.083		1.012	
15	60°	0.91	23.41	20.27	0.812	0.705	0.886	0.868	1.092	1.257
16			23.69	20.52	0.810	0.775	0.877	0.960	1.083	1.132
17 ¹⁾			23.67	20.50	0.810	0.868	0.889	1.071	1.098	1.024
18 ¹⁾			20.16	17.46	0.838	0.871	0.917	1.037	1.092	1.053
19 ¹⁾		1.50	22.10	19.14	0.823	0.825	0.908	1.000	1.102	1.101
20 ¹⁾			21.80	18.58	0.825	0.797	0.920	0.963	1.111	1.154
21		0.91	11.28	9.77	0.909	0.917	1.003	1.006	1.105	1.094
22			11.61	10.55	0.907	0.917	0.997	0.988	1.074	1.087
23			30.13	21.30	0.803	0.751	0.871	0.939	1.086	1.160
24			30.21	21.36	0.802	0.751	0.871	0.939	1.086	1.160
25	45°		30.79	21.77	0.798	0.763	0.865	0.957	1.083	1.134
26		30°	41.70	20.85	0.807	0.742	0.840	0.920	1.040	1.132
27			42.12	21.06	0.805	0.751	0.859	0.935	1.065	1.144
28			42.66	21.33	0.802	0.751	0.840	0.939	1.046	1.119
29 ¹⁾			40.20	20.10	0.814	0.880	0.892	1.083	1.098	1.014

- 1) specimen without a pre-fabricated fatigue crack
 2) LY12-CS aluminum alloy. Others are made of LY12-CZ aluminum alloy.
 3) specimen no.
 4) $\sigma_i(\text{net})/\sigma_{ys}$
 5) $\sigma_c(\text{net})/\sigma_{ys}$

During initiation and unstable growth, the uniform tensile stress σ_i and σ_c increase with increasing W/b (ratio of ductile belt width to plate width). For different angle of inclination β as long as the ductile belt width to plate width ratio W/b is close, i.e., when the projection of the crack along the direction perpendicular to the load $2a_0 (=2a \sin \beta)$ is close, the fracture stress σ_c is almost identical. Furthermore, in plane stress conditions, the average tensile stress during unstable growth σ_c is basically independent of the plate thickness.

3. Pre-fabricated Fatigue Crack

From the experimental data obtained with six specimens without pre-fabricated fatigue cracks shown in Table 2 one can see that their crack initiation load σ_i is very close to their instability load σ_c . There is a lack of an obvious steady-state crack growth stage. The instability load of specimens with pre-fabricated fatigue cracks, however, is apparently higher than the initiation load. Furthermore, there is an apparent steady-state crack growth process as shown in Figure 3.

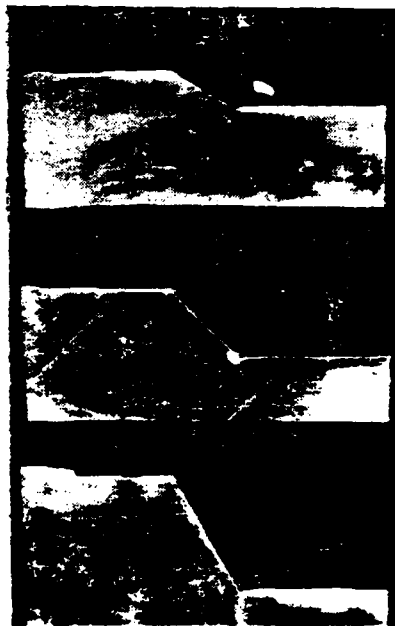
4. Crack Propagation Process

Figure 3a shows the results of the steady-state crack propagation process of three specimens (No. 19, 24 and 28) at $\beta = 60^\circ, 45^\circ$ and 30° , including the relation between uniform tensile stress σ with crack growth increment Δa . Figure 3b shows the $\sigma - \Delta a$ relations measured experimentally as well as calculated using the finite element method based on Mode I fracture (specimen 7) at $\beta = 90^\circ$ ^[6]. The calculated σ_c is in good agreement with the

experimental data. The error is less than 5%.

5. Direction of Crack Propagation

For center-cracked thin plate specimens with different angles of inclination β under tensile load, the crack propagates essentially in the same manner as that of a Mode I crack. It grows steadily along a direction perpendicular to the tensile direction until reaching an unstable state. Figure 4 shows the photographs of three failed specimens at $\beta=60^\circ$, 45° and 30° . The angle between the direction of crack propagation and the direction perpendicular to the load line (x-axis) is less than 10° .



■ 4

Figure 4

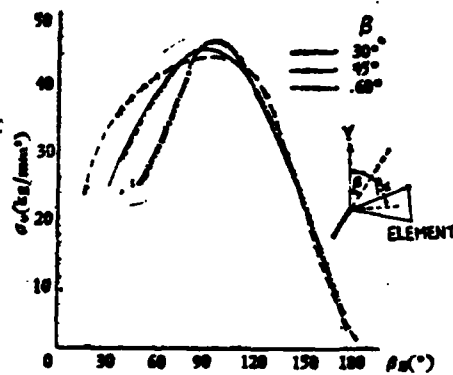


Figure 5. Specimens 19, 24 and 28
(Values of σ/σ_{ys} are 0.728, 0.711 and 0.712, respectively)

Figure 5 shows the tensile stress distribution, σ_θ , around the crack tip near the initiation load as calculated by the finite element method. In the element where the angle β_E with the y axis is close to 90° , σ_θ reaches its maximum value. This coincides with experimental observation of crack propagation perpendicular to the load direction.

In addition, based on the displacement field calculated, the relative displacement of the point approximately 0.4mm away from the crack top is named the crack top opening vector \vec{COD}_r (the numerical value of \vec{COD}_r is $\sqrt{u_x^2 + u_y^2}$ where u_x and u_y are relative displacements in x and y direction). The direction of \vec{COD}_r obtained from finite element calculation is near the load line direction. For specimens with $\beta=60^\circ$, 45° and 30° , the angle between \vec{COD}_r and the load line is approximately 4° - 10° . This

fact indicates that the estimated direction of crack propagation is essentially consistent with the experimental results.

6. Plastic Region

/501-

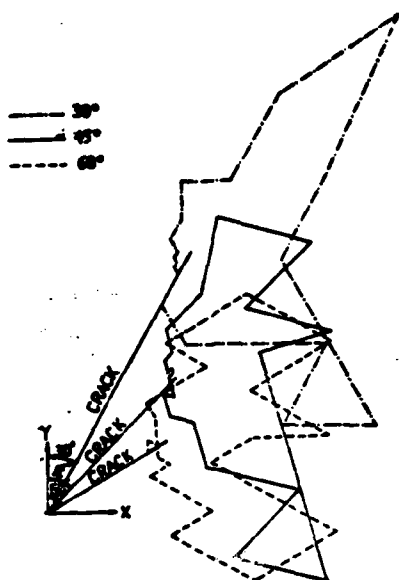


Figure 6. Specimens 19, 24 and 28
(σ/σ_{yz} values are 0.728, 0.711 and 0.712,
respectively)

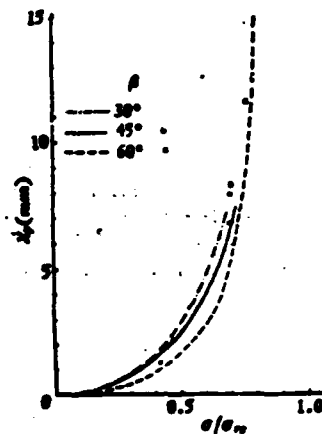


Figure 7. Specimens 19, 24 and 28

Figure 6 shows the plastic region distribution as calculated by the finite element method. Before the crack begins to propagate, the plastic region is already not quite small. The plastic regions in specimens with various angles of inclination β are similar in shape. The plastic region width on the ductile belt, x_p , is given in Figure 7. The calculated values obtained from finite element method agree well with the experimental data.

7. Strain Field

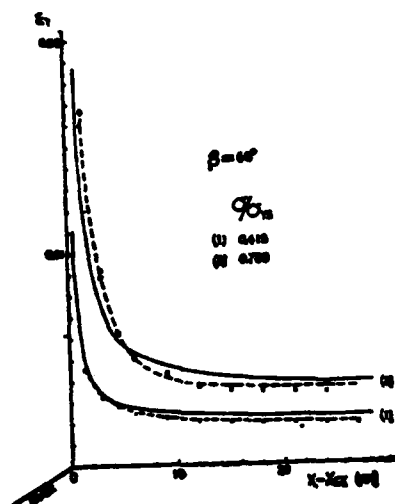


Figure 8. Specimen 19

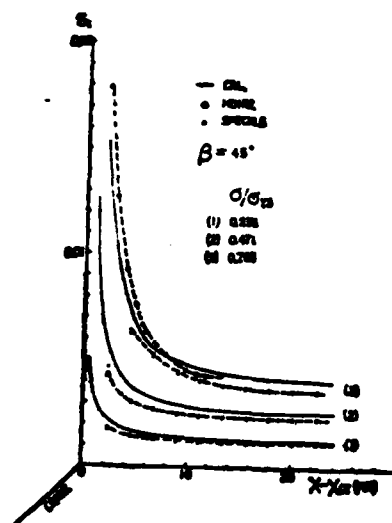


Figure 9. Specimen 24

The y-direction strain, ϵ_y , on the ductile belt is shown in⁵⁰² Figures 8 and 9. Results obtained by the laser speckle method and Moire's method agreed very well. In the figures, the experimental values are generally lower than the calculated results, primarily because the strain measured is an average between fringes and usually the spacing is larger than the dimension of the mesh used in a finite element method.

Both experimental and theoretical results show that the x-direction strain, ϵ_x , is much smaller than the strain in the tensile line y-direction, ϵ_y , for specimens with various angles of inclination. The computation also shows that shear strain on the ductile belt, γ_{xy} , is also much smaller than ϵ_y . Therefore, ϵ_y is the primary strain on the ductile belt.

In summary, under plane stress conditions, for center cracked specimens, the fracture stress is primarily determined by the ductile belt width to plate width ratio, W/b . This means that the fracture stress is determined by the projection of the crack in a direction perpendicular to the load line, $\overline{2a_0}$. Furthermore, it is basically independent of the plate thickness. In center cracked specimens of various angles of inclination β under uniform tensile load, the crack basically propagates perpendicular to the load line. The angle θ between the direction of cracking and the perpendicular direction, is less than 10° . After the crack is initiated, within a small range where the crack growth increment is less than the plate thickness, θ rapidly approaches 0° . In addition, ϵ_y , the strain

in the y-direction, is the primary strain on the ductile belt. These facts indicate that it is possible to adopt the Mode I elastic-plastic fracture model^[5] and the criterion of crack propagation in which the relative elongation reaches the elongation of the material^[6] to solve the plane stress mixed mode fracture problems.

References

- [1] Landes, J.D., Begley, J.S. and Clarke, G.A., Elastic-Plastic Fracture, ASTM STP668, American Society for Testing and Materials (1979).
- [2] Varanasi, S.R., In Flaw Growth and Fracture, ASTM, STP631, American Society for Testing and Materials (1977), 507-519.
- [3] Feddersen, C.E., Simonen, F.A., Hulbert, L.E. and Hyler, W. S., NASA CR-1678 (1970).
- [4] Xue Yinian, Han Jinhu and Xu Jilin, Experimental Study of Steady-state Crack Propagation on Thin Aluminum Alloy Plate With Center Crack, Journal of Solid State Mechanics, 1 (1984).
- [5] Xu Jilin and Wang Ziqiang, Elastic-plastic Fracture Model of Plane Stress and Its Finite Element Analysis, Journal of Solid State Mechanics, 2 (1980), 183.
- [6] Xu Jilin, Finite Element Analysis Using Elastic-plastic Deformation on Steady-state Crack Propagation Under Plane Stress, Journal of Mechanics, 3 (1982), 272.

- [7] Ueda, Y., Ikeda, K., Yao, T., Aoki, M., Shibasaki, S. and Shirakura, T., in *Advances in Fracture Research*, ICF5, 5 (1981), 2321-2328.
- [8] Xue Yinian and Han Jinhu, Measuring Crack Opening Displacement of Cracked Thin Plate Using Laser Speckle Method and Moire's Method, *Journal of Mechanics*, 5 (1981), 501.

AN ELASTIC-PLASTIC MIXED MODE FRACTURE INVESTIGATION FOR PLANE STRESS

Xu Jilin, Xue Yinian, Han Jinhu
(Institute of Mechanics, Academia Sinica)

Abstract

In this paper the stable crack growth processes in aluminium alloy sheet specimens with flat or inclined central crack, subjected to uniform tensile load have been investigated. The relation between the tensile load and the amount of crack extension was obtained. The deformation field was measured by using laser speckle method and Moire' method. Finite element analysis based on large elastic-plastic deformation equation has also been carried out. The criterion proposed to predict crack growth under mode I condition is that^m the tensile strain at the crack tip reaches the maximum elongation of material. The calculated results are in good agreement with the experiment data.

An Analytical Solution of Dynamic Response for Ideal Rigid
Plastic Timoshenko Beam

/504

Jin Quanlin

(Research Institute of Mechanical and Electrical Technology,
Ministry of Machine Building Industry)

Abstract

In this paper, an analytical solution for a fixed-ended Timoshenko beam under uniform dynamic load is given by using different discontinuity conditions for various states of motion at the rigid plastic interface. This solution is applicable to any non-reversing load which varies with time. At the end, the effect of the rotational inertia on the dynamic response of the beam is discussed.

I. Introduction

In recent years quite a few people have studied the influence of shear effect and rotational inertia on the plastic dynamic response of the beam^[5-8]. Jones^[2-4] summarized these results. However, their studies are limited to dealing with the initial velocity problem which is equivalent to the immediate unloading after instantaneous loading. It is very important to use the discontinuity condition accurately. To this end, reference [1] was the first paper to discuss it theoretically. It was pointed out that different discontinuity conditions should be used for different directions of motion on the discontinuity

plane. In this paper, a fixed-ended Timoshenko beam under a uniform load is used as an example to solve the problem states of motion at a rigid plastic interface. Furthermore, the transformation condition from one state to another is given. Therefore, the solution given in this work is applicable to any non-reversing time-varying load.

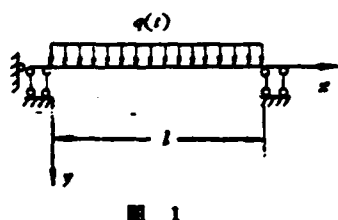


Figure 1

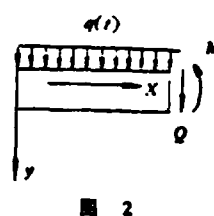


Figure 2

II. Basic Equations

Let us consider a fixed-ended (neglecting axial force), equi-sectional ideal plastic beam which is l in length and is under a uniform dynamic load $q(t)$ (see Figure 1). Its mass per unit length is m , and the rotational inertia is r . The bending moment and shear force on the cross-section of the beam are M and Q , respectively. (The positive directions are shown in Figure 2). The deflection of the beam is y . The angle of inclination caused by the bending deformation of the beam is ϕ . x is used to represent the abscissa of the beam cross-section. The equation

of motion of the beam is

$$\dot{Q}' = m\dot{\gamma} - q, \dot{M}' = Q - m\dot{x}\ddot{\phi}. \quad (1)$$

where the dots on top of the letters and the quotation mark on the upper right corners of the letters are the partial derivatives of time t and x . The total angle inclination of the beam is $\gamma' = \phi + \gamma$, where γ is the rotation angle caused by shear deformation. Furthermore, it is specified that the rotation of ϕ and γ in the positive direction

Manuscript received on December 7, 1982.

makes $\gamma' > 0$.

/505

Let us introduce the following non-dimensional quantities:

$$\bar{M} = M/M_0, \bar{Q} = Q/Q_0, \mu = ql^2/2M_0, \beta = Q_0/M_0, \alpha = \left(\frac{r}{l}\right)^2, \\ \bar{\gamma} = \frac{ml^2}{T^2M_0}\gamma, \bar{\phi} = \frac{ml^3}{T^2M_0}\phi, \bar{k} = \frac{ml^4}{T^2M_0}k, \bar{r} = \frac{ml^3}{T^2M_0}r, \bar{x} = \frac{x}{l}, \bar{\zeta} = \frac{\Delta}{l}, \bar{t} = \frac{t}{T}.$$

where M_0 and Q_0 are the limiting bending moment of pure bending yield of the beam cross-section and the limiting shear force of pure shear yield, respectively. Δ is the x -coordinate at the rigid plastic interface. $K = \phi'$ is the curvature of bending of the beam. T is a unit time. In the following, for convenience, the bars on top of \bar{M} , \bar{Q} , \bar{t} , \bar{x} , $\bar{\phi}$, \bar{k} and $\bar{\gamma}$ are omitted. They are expressed as non-dimensional quantities. Equation (1) is rewritten as:

$$\beta Q' = \gamma - 2\mu, \quad M' = \beta Q - \alpha \ddot{\phi} \quad (2)$$

Let us choose a square yield plane as shown in Figure 3. In the plastic region, equation (2) is solved by using the yield condition and the relevant orthogonal flow method. When stress

AD-A162 726

ACTA MECHANICA SINICA (SELECTED ARTICLES) (U) FOREIGN
TECHNOLOGY DIV WRIGHT-PATTERSON AFB OH X YIN ET AL.
05 DEC 85 FTD-ID(RS)T-0494-85

2/2

UNCLASSIFIED

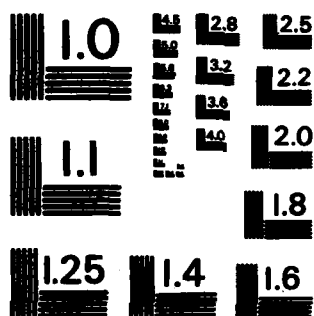
F/G 20/4

NL

END

FORMED

DTIC



MICROCOPY RESOLUTION TEST CHART
NATIONAL BUREAU OF STANDARDS-1963-A

points are located on the side AB or CD of the yield plane,

$$\dot{y} = C_1(x) \frac{x}{\sqrt{a}} + C_2(x) \frac{x}{\sqrt{a}} + 2\mu. \quad (3)$$

When the stress points are located on the side AC or BD on the yield plane,

$$\dot{y} = 2\mu \quad (4)$$

In the rigid region, we have

$$\dot{y} = C_3(t)x + C_4(t) \quad (5)$$

In order to determine C_1 , C_2 , C_3 and C_4 in these equations, it is necessary to know the boundary condition of the beam and the following discontinuity condition^[1] at the rigid plastic interface:

When the motion of the rigid plastic interface leads to the expansion of the plastic region,

$$[y] = [\dot{\phi}] = 0 \text{ and } [Q] = [M] = 0 \quad (6)$$

When the motion of the rigid plastic interface leads to the contraction of the plastic region,

$$[y] = [\dot{\phi}] = 0 \text{ and } [Q] = [M] = 0 \quad (7)$$

$[z] = z^+ - z^-$ which is the discontinuity value of a physical quantity z at the rigid plastic interface. z^+ and z^- are the values of the physical quantity on the plastic and rigid region, respectively (same below). Under the assumption of square yield, the orthogonal flow method and equations (16) and (32) in reference [1] are used. When the rigid plastic interface is stationary, if the stress points on the plastic side are located on AB or CD of the yield plane, then we have

$$[\dot{y}] = 0 \text{ and } [Q] = [M] = 0 \quad (8)$$

If the stress points on the plastic side are located on AC or BD of the yield plane, then we have

$$[\ddot{\phi}] = 0 \text{ and } [Q] = [M] = 0 \quad (9)$$

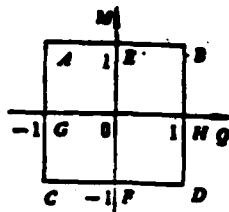


Figure 3

Figure 3

III. Dynamic Analysis

Assuming that the yield plane is square, the results of rigid plastic limit analysis (taking shear effect into account) of a fixed-ended beam under uniform load give the initial mechanistic phase diagram as shown in Figure 4(c). When $\mu \leq \beta$ and $0 \leq \mu \leq 8$, the beam is stationary. When $0 \leq \beta \leq 8$ and $\mu|_{t=0} = \mu(0) > \beta$, the beam slides with respect to the support. The solution is easy to find and it is independent of α . When $\beta > 8$ and $\mu(0) > 8$, there is a plastic region in the middle of the beam. The stress points are located on side AB(non-corner) of the yield plane. The region between this region and the end of the beam is the rigid region. When the beam end is a plastic hinge, and stress points are on side CD, if stress points are at the corners C and D, then the

beam at the end not only rotates but also slides. Otherwise, the beam only rotates. In the following, we will discuss the situation $\mu(0) > 8$ and $\beta > 8$. Because of symmetry, only the left half of the beam is discussed.

/506

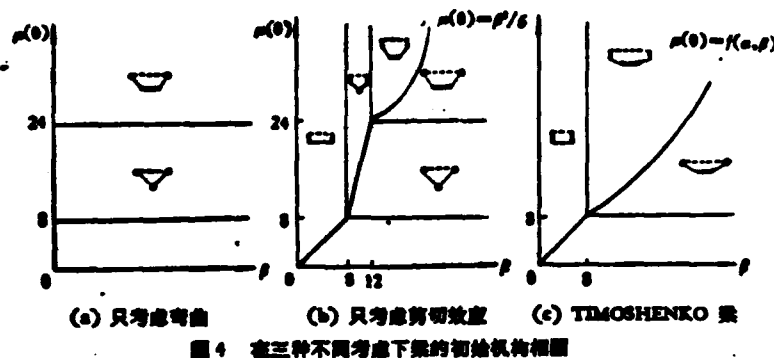


Figure 4. Initial Mechanistic Phase Diagram of the Beam Under Three Different Considerations

- (a) considering bending alone
- (b) considering shear effect
- (c) Timoshenko beam

Let us assume that $\dot{y}|_{t=0} = y|_{t=0} = 0$. The boundary conditions are: $M|_{x=0} = -1$, $Q|_{x=\frac{1}{2}} = 0$. Furthermore, when $\dot{y}_a = y|_{x=0} > 0$, $Q_a = Q|_{x=0} = 1$. From equations (2), (3), (5) and boundary conditions, we get the following solution:

In the rigid region ($0 \leq x \leq \xi$):

$$\left. \begin{aligned} \dot{y} &= \dot{y}_0 + \dot{\phi}_0 x, \quad y = y_0 + \dot{\phi}_0 x \\ \beta Q &= \beta Q_0 - (2\mu - \dot{y}_0)x + \frac{1}{2} \dot{\phi}_0 x^2 \\ M &= -1 + (\beta - \alpha \dot{\phi}_0)x - \frac{1}{2} (2\mu - \dot{y}_0)x^2 + \frac{1}{6} \dot{\phi}_0 x^3 \end{aligned} \right\} \quad (10)$$

In the plastic region ($\xi \leq x \leq \frac{1}{2}$):

$$\dot{y} = \dot{C} \operatorname{ch} \frac{x-1/2}{\sqrt{\alpha}} + 2\mu, \quad \beta Q = \dot{C} \sqrt{\alpha} \operatorname{sh} \frac{x-1/2}{\sqrt{\alpha}}, \quad M = 1 \quad (11)$$

where ϕ_a represents the non-dimensional value of the angle of rotation in the rigid region.

(1) When $\dot{\gamma}_a=0$ and $\xi<0$, by substituting equations (10) and (11) into the discontinuity condition (6) to simultaneously solve the problem:

$$\left. \begin{aligned} C &= \frac{\sqrt{a}}{B} 2\mu, \quad \bar{C}_0 = \frac{2\mu}{B} \operatorname{ch} \frac{\xi-1/2}{\sqrt{a}}, \\ \rho Q_0 &= \left[\left(a + \frac{1}{2} \xi^2 \right) \operatorname{ch} \frac{\xi-1/2}{\sqrt{a}} - \sqrt{a} \xi \operatorname{ch} \frac{\xi-1/2}{\sqrt{a}} \right] \cdot \frac{2\mu}{B}, \\ \xi^2 &= \left[\left(\frac{1}{2} - \frac{1}{3} \xi \operatorname{ch} \frac{\xi-1/2}{\sqrt{a}} / B \right) \cdot \mu \right]^{-1}, \\ \xi &= -\mu/(\mu^2 \eta), \quad \xi|_{\xi=0} = -\bar{\mu}/(\mu^2 \eta). \end{aligned} \right\} \quad (12)$$

where

$$\begin{aligned} B &= \xi \operatorname{ch} \frac{\xi-1/2}{\sqrt{a}} - \sqrt{a} \operatorname{ch} \frac{\xi-1/2}{\sqrt{a}}, \\ \eta &= \frac{\xi}{B} \left[\left(a + \frac{1}{3} \xi^2 \right) \operatorname{ch} \frac{\xi-1/2}{\sqrt{a}} - \xi \sqrt{a} \operatorname{ch} \frac{\xi-1/2}{\sqrt{a}} \operatorname{ch} \frac{\xi-1/2}{\sqrt{a}} \right] > 0. \end{aligned} \quad (A)$$

From $\dot{\phi}_a|_{t=0} > 0$, $Q_a \leq 1$ and $\xi < 0$, we get

$$\mu(0) = \mu|_{\xi=0} > 8, \quad \mu \leq \mu_1, \quad \mu > 0 \quad (13)$$

where

$$\left. \begin{aligned} \mu_1 &= 2(\beta \xi_1^2 - 3\xi_1^2 + 6a)/[\xi_1^2(\xi_1^2 + 6a)], \\ \operatorname{ch} \frac{\xi_1-1/2}{\sqrt{a}} &= 3\sqrt{a} \xi_1(\beta \xi_1 - 4)/(\beta \xi_1^2 - 6\xi_1^2 - 12a) \end{aligned} \right\} \quad (14)$$

Obviously, $\xi_1 \leq \xi$. When $\mu(0) \leq 8$, $\dot{\gamma}_a=0$. When $\mu > \mu_1$, $Q_a=1$ and $\dot{\gamma}_a > 0$.

When $\dot{\mu}=0$, $\dot{\xi}=0$.

(2) When $\dot{\gamma}_a=0$ and $\xi>0$, by substituting equations (10) and (11) into the discontinuity condition (7), we get the solution:

$$\begin{aligned}
C &= \int_0^t C d\tau = \frac{\sqrt{a}}{B} D, \quad \phi_0 = \frac{D}{B} \operatorname{ch} \frac{\xi-1/2}{\sqrt{a}} + v'(\xi) \\
C &= \frac{\sqrt{a}}{B} 2\mu - \xi \xi E, \quad \phi_0 = \frac{2\mu}{B} \operatorname{ch} \frac{\xi-1/2}{\sqrt{a}} - \xi \operatorname{ch} \frac{\xi-1/2}{\sqrt{a}} E, \\
PQ_0 &= \left[\left(a + \frac{1}{2} \xi^2 \right) \operatorname{ch} \frac{\xi-1/2}{\sqrt{a}} - \sqrt{a} \xi \operatorname{ch} \frac{\xi-1/2}{\sqrt{a}} \right] \cdot \frac{2\mu}{B} \\
&\quad - \xi \xi \left(\sqrt{a} \operatorname{ch} \frac{\xi-1/2}{\sqrt{a}} - \frac{1}{2} \xi \operatorname{ch} \frac{\xi-1/2}{\sqrt{a}} \right) E, \\
\xi^2 &= \left[2\tau - \frac{1}{3} \xi \phi_0 - \int_0^t (v(\xi) - av''(\xi)) \xi d\xi \right] / \\
&\quad \left[\int_0^t \mu d\tau - \frac{1}{3} \xi \left(\frac{D}{B} \operatorname{ch} \frac{\xi-1/2}{\sqrt{a}} + v'(\xi) \right) \right], \\
\xi &= \left[\int_0^t \mu d\tau - \mu\tau + \frac{1}{2} \mu f(\xi) \right] / \left[\left(\int_0^t \mu d\tau \right)^2 (\eta + \eta_1) \right] \\
\xi &= \left\{ -\mu \left(\tau - \frac{1}{2} f(\xi) \right) + \xi \left[2\mu \left(\frac{1}{4} f(\xi) - (\eta + \eta_1) \int_0^t \mu d\tau \right) \right. \right. \\
&\quad \left. \left. - \xi (\eta'(\xi) + \eta_1'(\xi)) \cdot \left(\int_0^t \mu d\tau \right)^2 \right] \right\} / \left[\left(\int_0^t \mu d\tau \right)^2 (\eta + \eta_1) \right]
\end{aligned} \tag{15}$$

where $\tau = t - t_0$, and t_0 is the initial time of the initial state.

$$\begin{aligned}
\xi_0 &= \xi|_{\tau=0}, \quad v = v|_{\tau=0}, \quad \phi_0 = \phi_0|_{\tau=0}, \quad D = \int_0^t 2\mu d\tau + v(\xi) - \xi v'(\xi), \quad E = \left[\operatorname{ch} \frac{\xi-1/2}{\sqrt{a}} \cdot D/B + \sqrt{a} v''(\xi) \right] / B, \\
\eta_1 &= \xi \cdot \left[\frac{1}{3} \xi^2 \operatorname{ch} \frac{\xi-1/2}{\sqrt{a}} / B - \sqrt{a} \right] \cdot \left[\operatorname{ch} \frac{\xi-1/2}{\sqrt{a}} (v(\xi) - \xi v'(\xi)) / B + \sqrt{a} v''(\xi) \right] / \left(\int_0^t 2\mu d\tau \right), \\
f(\xi) &= \frac{1}{3} \xi^2 \phi_0 - \frac{1}{3} \xi^2 \left[v(\xi) \operatorname{ch} \frac{\xi-1/2}{\sqrt{a}} - \sqrt{a} v'(\xi) \cdot \operatorname{ch} \frac{\xi-1/2}{\sqrt{a}} \right] / B + \int_0^t (v(\xi) - av''(\xi)) \xi d\xi.
\end{aligned}$$

Notice that $\dot{y}|_{t=0}=0$. By mathematical deduction we can prove

that: at any t , we have $v > 0$, $v' > 0$, $v'' < 0$ and $v'|_{x=\frac{1}{2}} = 0$. Hence, $\eta_1 >$

0 , $f(\xi) \geq 0$. By using $\phi_a|_{\xi=\frac{1}{2}} = \phi_a|_{\xi=\frac{1}{2}} = 0$, $\psi_a|_{r=t=0} > 0$, based on $\psi_a \geq 0$ and $\xi > 0$.

can obtain:

$$\mu(0) > 0, \quad \mu(\tau) = \frac{1}{\tau} \int_0^t \mu d\tau \geq \mu_1, \quad \mu(\tau) > \mu_1 \tag{16}$$

where

$$\mu_1 = 0 - \frac{4}{\tau} \left[\frac{1}{3} \xi \phi_0 + \int_0^t (v(\xi) - av''(\xi)) \xi d\xi \right], \quad \mu_1 = \mu(\tau) \left(1 - \frac{1}{2} f(\xi) \right).$$

When $\mu(0) \leq 8$, $\dot{y}_a = 0$. When $\bar{\mu}(\tau) = \mu_*$, the beam reaches its maximum deflection. When $\bar{\mu}(\tau) = \mu_*$, $\xi = 0$. If $Q_a = 1$, we get $\xi = \xi_0 = \xi_1$, which is a contradiction to $\xi > 0$. Therefore, $Q_a|_{\tau > 0} < 1$. Furthermore, $\dot{y}_a = 0$ and $\xi \geq \xi_1$.

(3) When $\dot{y}_a = 0$ and $\dot{\xi} = 0$, we will first prove that $[\dot{\phi}] = 0$ when $\dot{\xi} = 0$ and then discuss the solution in this situation.

Let us assume that $\dot{\xi} = 0$ when $t_1 \leq t < t_2$ and $\dot{\xi} \neq 0$ when $t < t_1$ or $t > t_2$. Note that $\bar{A} = 2\mu - \dot{y}_a$ and $\xi|_{t=t_1} = \xi_0$. When $t_1 < t < t_2$, equations (10) and (11) are substituted into the discontinuity equation (8) to solve \bar{C} and $\bar{\phi}_a$. Then we get:

$$[\dot{\phi}] \propto \left\{ \beta Q_a - 2 \left[\xi + \left(a - \frac{1}{2} \xi^2 \right) \operatorname{sh} \frac{\xi - 1/2}{\sqrt{a}} / B_0 \right] / \left[\xi^2 \left(\frac{1}{2} - \frac{1}{3} \xi + \frac{\xi - 1/2}{\sqrt{a}} / B_0 \right) \right] \right\} \quad (17)$$

where

$$B_0 = \xi_0 \operatorname{sh} \frac{\xi_0 - 1/2}{\sqrt{a}} - \sqrt{a} \operatorname{ch} \frac{\xi_0 - 1/2}{\sqrt{a}}$$

If $t_2 > t_1$ and $\dot{y}_a = 0$, we get $\dot{\xi} = 0$ when $t_1 < t < t_2$. From equations (12) and (15) we get $\dot{\mu}|_{\xi=0} \lim_{\xi \rightarrow 0} \dot{\mu} \lim_{\xi \rightarrow 0} \dot{\mu} = 0$, i.e., $\dot{\mu} = \mu|_{t=t_1} = \mu|_{t=t_2}$. βQ_a obtained from equation (8), however, is only a function of μ and ξ_0 . Hence, $\beta Q_a = \beta Q_a|_{t=t_1} = \beta Q_a|_{t=t_2}$. In the two cases that $t_2 > t$, $\dot{y}_a > 0$ and $t_2 = t_1$, this equation is obviously valid.

By using the reverse method we can prove that if $\dot{y}_a > 0$ we have $\dot{\xi} = 0$. Hence, when $t < t_1$ or $t > t_2$, $\dot{y}_a = 0$. Its solution can be expressed by equation (12) or (15). When $\dot{\xi} \rightarrow 0$, we have

$$\beta Q_a \rightarrow 2\mu \left[\xi + \left(a - \frac{1}{2} \xi^2 \right) \operatorname{sh} \frac{\xi - 1/2}{\sqrt{a}} / B \right],$$

$$\bar{\phi}_a \rightarrow \frac{2\mu}{B} \operatorname{sh} \frac{\xi - 1/2}{\sqrt{a}},$$

Notice that

$$[M] = 2 - (\rho Q_0 - \alpha \dot{\xi}_0) \xi + \mu \xi^2 - \frac{1}{6} \dot{\xi}_0 \xi^2 = 0,$$

$$\lim_{\xi \rightarrow 0} \left[\xi \left(\frac{1}{2} - \frac{1}{3} \xi \operatorname{sh} \frac{\xi - 1/2}{\sqrt{\alpha}} / B \right) \right] = \frac{1}{\mu}.$$

Therefore:

$$\rho Q_0 - \rho Q_0|_{\xi=0} = \lim_{\xi \rightarrow 0} \rho Q_0 - \lim_{\xi \rightarrow 0} \rho Q_0 = 2 \frac{\xi_0 + \left(\alpha - \frac{1}{2} \xi_0 \right) \operatorname{sh} \frac{\xi_0 - 1/2}{\sqrt{\alpha}} / B_0}{\xi_0 \left(\frac{1}{2} - \frac{1}{3} \xi_0 \operatorname{sh} \frac{\xi_0 - 1/2}{\sqrt{\alpha}} / B_0 \right)} \quad (18)$$

By substituting equation (18) into (17) we get $[\dot{\xi}] = 0$. Thus, we /509
proved that discontinuity condition (6) could be used when $\dot{\xi} = 0$.
Hence, when $\dot{y}_a = 0$ and $\dot{\xi} = 0$, the solution of the problem is the same
as equation (12). Furthermore, the necessary condition to
maintain the initial state: $\mu(0) > 8$, $\mu < \bar{\mu}$, and $\dot{\mu} = 0$.

(4) When $\dot{y}_a > 0$, $Q_a = 1$. As described above, $\dot{\xi} = 0$. By using
discontinuity condition (6) we get

$$\xi = \xi_1, \quad \dot{\xi} = \frac{\sqrt{\alpha}}{B_1} 2\mu_1, \quad \dot{\xi}_0 = \frac{2\mu_1}{B_1} \operatorname{sh} \frac{\xi_1 - 1/2}{\sqrt{\alpha}}, \quad \dot{y}_0 = 2(\mu - \mu_1) \quad (19)$$

where $B_1 = \xi_1 \operatorname{sh} \xi_1 - \frac{1}{2} \sqrt{\alpha} - \sqrt{\alpha} \operatorname{ch} \xi_1 - \frac{1}{2} \sqrt{\alpha}$. Note that $\tau = t - t_1$ and t_1 is
the starting time of the initial state. From $\dot{y}_a|_{\tau=0} > 0$, $\dot{y}_a|_{\tau=0} = 0$
and $\dot{y}_a|_{\tau>0} > 0$, we get:

$$\mu|_{\tau=0} > \mu_1, \quad \mu(\tau) = \frac{1}{\tau} \int_0^\tau \mu d\tau > \mu_1. \quad (20)$$

When $\bar{\mu} = \mu_1$, $\dot{y}_a = 0$, $\dot{y}_a < 0$. It was pointed out earlier that when $\dot{y}_a = 0$
we have $\xi \geq \xi_1$. Afterwards, it enters the state of $\dot{y}_a = 0$ and $\xi \geq 0$.

The above discussion is applicable to problems with
uniformly distributed initial velocity as long as we make $\mu(0) \rightarrow \infty$
 $\mu|_{t>0} = 0$ and $\int_0^t 2\mu dt = \dot{y}|_{t=0}$.

IV. Results and Discussion

Table 1. External Total Impulse Load (10 Ib s)

表 1 外载总冲量 (10 Ib s)

1. 载荷曲线							5. 初速问题
2. 最大载荷 (Ib/in)	0.1×10^3	0.1×10^3	0.1×10^3	0.5×10^3	0.1×10^3	0.1×10^3	6. 初速度为: $0.2732(\text{in/s})$
3. 载荷作用时间 (s)	0.2×10^{-3}	0.2×10^{-3}	0.2×10^{-3}	0.2×10^{-3}	0.2×10^{-3}	0.2×10^{-3}	
4. 中点最大挠度 (in)	1.44112	1.99078	2.04280	1.42183	2.95834	2.74981	1.61766

1. load curve
2. maximum load (Ib/in)
3. duration during which load is applied (s)
4. maximum deflection in the middle (in)
5. initial velocity problem
6. initial velocity is: $0.2732(\text{in/s})$.

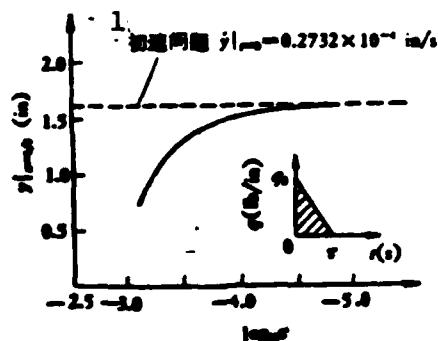


Figure 5. Middle Beam Deflection vs. Duration of Loading When Total Impulse and Loading Mode Are Identical

1. initial velocity problem $\dot{y}/_{t=0} = 0.2732 \times 10^{-4} \text{ in/s}$

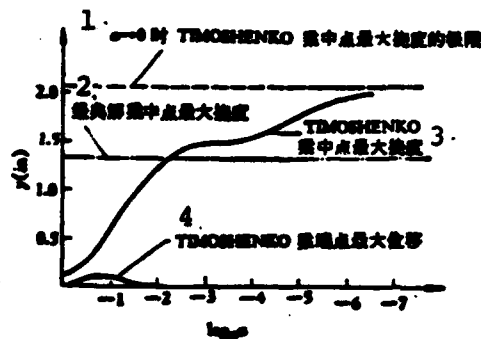


Figure 6. Maximum Deflection Middle and End of Beam vs. α

1. maximum limit of deflection in the middle of Timoshenko beam when $\alpha \rightarrow 0$
2. maximum deflection at the middle of the beam according to classical solution
3. maximum middle deflection of Timoshenko beam.
4. maximum end point displacement of Timoshenko beam (beam parameters are same as those in Figure 12)

1. From the results tabulated in Table 1 we can see that the maximum deflection at the middle of the beam is different when the total external impulse load is the same but the loading mode is different. Figure 5 shows the middle beam deflection vs. loading time curve when the total external impulse and the loading mode are identical. We can see that when the loading time approaches zero, the maximum deflection at the middle point of the beam approaches the corresponding value of the initial velocity problem. /510

2. Rotational inertia and shear effect have an obvious effect on the mechanism of the motion of the beam. Figure 4 shows the initial mechanistic phase diagrams of the fixed-ended

beam under the different considerations to explain this effect. In Figure 4(c), the curve $\mu(0)=f(\alpha, \beta)$ separating the rotational mechanism from the rotational and sliding mechanism is given in the following equation (they are obtained by changing μ_1 to $\mu(0)$ in equation (14)).

$$\mu(0) = 2(\beta E_1^2 - 3E_1^2 + 6\alpha) / [E_1^2(E_1^2 + 6\alpha)]$$

$$\ln \frac{E_1 - 1/2}{\sqrt{\alpha}} = 3\sqrt{\alpha} E_1 (\beta E_1 - 1) / (\beta E_1^2 - 6E_1^2 - 12\alpha)$$

3. Effect of Rotational Inertia on Maximum Deflection

In reference [6], Jones showed Figure 7 to explain the effect of rotational inertia on the maximum deflection of the beam in initial velocity problems. In this paper, after considering the load, the results are shown in Figures 6 and 7. From Figure 6 we can see that under a specific load, without changing other beam parameters, the larger the value of α is, the smaller the mid point deflection is. When α increases to a specific value, shear slide begins at the end point of the beam. When α approaches zero, the maximum deflection of the middle of the beam approaches a limiting value. However, this value is higher than the maximum deflection given by the classical solution in which only the effect of bending is considered. This situation can be explained as follows:

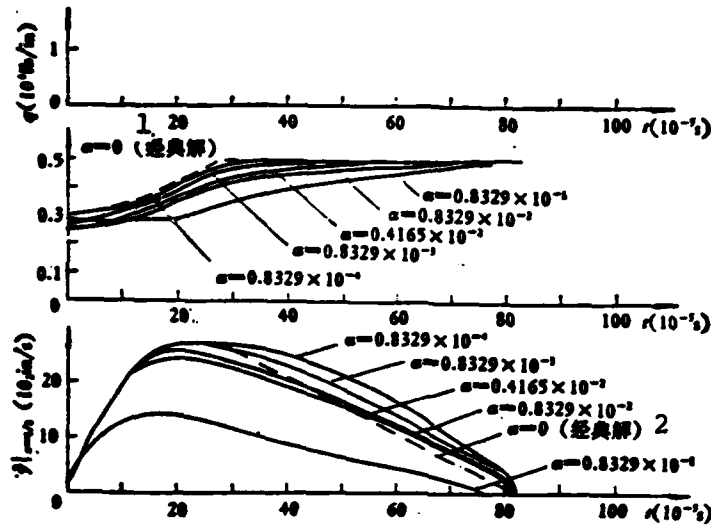


Figure 7. Rigid Plastic Interface Plane Positions ξ and Mid Beam Velocity vs. Time with Different Rotational Inertia

Beam parameters: $M_0 = 0.191 \times 10^4$ Ibin; $Q_0 = 0.880 \times 10^4$ Ib, $m = 0.366 \times 10^{-3}$ Ibs²/in, $l = 5$ in, $\beta = 0.231 \times 10^2$, (when $\alpha = 0.8329 \times 10^{-3}$, it is equivalent to a square cross-section beam with uniform mass distribution, $\sigma_0 = 30.5 \times 10^3$ Ib/in², $\tau_0 = \sigma_0 / \sqrt{3}$, $\rho = 0.732 \times 10^{-3}$ Ibs²/in³, $h = 0.5$ in and $b = 1$ in, where σ_0 , τ_0 , and ρ are the unit tensile yield stress, shear yield stress and density of the beam material, and h and b are the height and width of the beam cross-section).

1. classical solution
2. classical solution

From Figures 7(b) and (c) we can see that when α is very small, ξ , the time to reach maximum deflection t_f and the mid point velocity $\dot{y}|_{x=\frac{1}{2}}$ when $t < t_s$ given by this solution and those given by the classical solution are very close. Here, t_s represents $\xi = \frac{1}{2}$ in the classical solution. However, when $t > t_s$, the values of $\dot{y}|_{x=\frac{1}{2}}$ given by the two solutions are quite different.

This solution gives

/511

$$\dot{y}|_{x=\frac{1}{2}} = \left(\frac{\sqrt{\alpha}}{B} + 1 \right) \int_0^t 2\mu ds, \quad (t \geq t_s), \quad \alpha \rightarrow 0,$$

Let $\alpha \rightarrow 0$, we get

$$\dot{y}|_{x=\frac{1}{2}} = \int_0^t 2\mu ds, \quad (t \geq t_s).$$

The classical solution gives $\dot{y}|_{x=\frac{1}{2}} = \int_0^{\tau} 2\mu dt - 24(t - t_s)$, and $(t \geq t_s)$. Here, τ is the duration over which the external load is applied. It is obvious that the former is a uniform motion and the latter is a uniform deceleration motion. These two equations are integrated to obtain the maximum deflections of the two solutions at the middle of the beam. In this example, they differ by 36.3%.

This work was completed under the guidance of Professor Wang Ren. Our teacher Huang Zhuping also assisted. The authors wish to express their gratitude.

References

- [1] Huang Zhuping "Discontinuity in Ideal Rigid-Plastic Dynamic Analysis", Journal of Mechanics, 5 (1983).
- [2] Jones, N., Shock Vib. Dis. 7B (1975), 89-105.
- [3] Jones, N., Shock Vib. Dis, Part I, 10, 9 (1978), 21-23; Part 2, 10, 10 (1978), pp. 13-19.
- [4] Jones, N., Inst. Phys. conf. ser. No. 47: ch. 3.
- [5] Karunes, B. and Onat, E.T., ASME. J. Appl. Mech., 27 (1960), 107-110.
- [6] Jones, N., ASME. J. Appl. Mech. 46, 2 (1979), 303-310.
- [7] Dikovich, I.L. Dynamics of elastic-plastic beams (1960).
- [8] Symonds, P.S., Engineering plasticity, edited by J. Heyman and F.A. Leckie, C.U.P. (1968).

AN ANALYTICAL SOLUTION OF DYNAMIC RESPONSE FOR THE RIGID PERFECTLY PLASTIC TIMOSHENKO BEAM

Jin Qianlin

(Research Institute of Mechanical and Electrical Technology Ministry of Machine-Building Industry)

Abstract

Previous studies on Timoshenko beam was only dealt with for impulsive velocity but not for increasing load. An analytical solution of dynamic response for the fixed-ended Timoshenko beam subjected to uniformly distributed dynamic load is given herein by use of the discontinuity conditions for moving rigid-plastic interface. The solution is valid for arbitrarily time-varying but non-reversing load. Finally the influence of rotatory inertia on the dynamic plastic response of beams is discussed.

General Variational Theorem for Structural Plastic Buckling /512

Analysis Using Deformation Theory

Li Guochen

(Institute of Mechanics, Academia Sinica)

Abstract

This paper gives a class of general variational theorem to analyze structural plastic buckling using deformation theory, which explains the essential significance of potential energy. In the form of general variation, we proved that there is no unloading during plastic buckling. Finally, it was applied to examples in the analysis of reinforced plate and shell.

Introduction

As we know, in the structural analysis of plastic buckling, it is more appropriate to use the increment theory of Prandtl-Reuss to describe the stress-strain relation. The results are even more close to the experimental data.

Regardless of whether it is elastic buckling or plastic buckling, the analysis must be carried out in two parts. One is to find the basic solution prior to buckling. Second is to see whether there is another path at any point on the basic route. When conducting the buckling analysis, Hill^[1] used a "comparative elastic solid" model, i.e., there is no unloading at the instance of buckling. Hutchinson^[2] analyzed the second order generalized function consisting of displacement variables based on the uniqueness of Hill's solution^[1] to further verify

this problem. Bushnell^[3] used a difference method to calculate many structural buckling problems and he claimed that the no unloading phenomenon is a condition for "consistent loading". The history of this condition was also introduced in reference [3].

The computation of plastic buckling is far more complicated than that of elastic buckling. In order to simplify the problem to the extent possible, the variational principle is a powerful tool. Referring to the generalized variational theorem^[4] under elastic conditions developed by Reissner, this paper gives a general variational theorem in the analysis of structural buckling using deformation theory. The physical significance of the generalized function and its second order variation involved is explained. The basis of "consistent loading" used in this general variational theorem was further proved. Finally, the superiority of this general variational theorem was demonstrated in simplifying the basic equations of plate and shell structures.

I. A Class of General Variational Theorem

Let us assume that the generalized potential energy is

$$\Pi = \int_V [\sigma_{ij} \epsilon_{ij} - V(\sigma_{ij})] dV - \int_{\sigma_T} \bar{T}_i u_{i,T} d\sigma_T \quad (1)$$

where σ_{ij} is the stress tensor, ϵ_{ij} is the strain tensor which is related to displacement according to the following known relation

$$\epsilon_{ij} = \frac{1}{2} (u_{i,j} + u_{j,i}) + \frac{1}{2} u_{k,l} u_{k,l}$$

Here, the comma in front of a subscript represents the differentiation with respect to that subscript. \bar{T}_i is the known externally applied stress on the surface s_T .

Manuscript received on September 2, 1983.

/513

$$\nu = \frac{1-2\nu}{6E} (\sigma_{kk})^2 + \frac{1+\nu}{3E} \sigma_e^2 + \frac{2}{3E} \int_{\sigma_e}^{\sigma_e} \phi \sigma_e d\sigma_e$$

Here

$$\sigma_{kk} = \delta_{ij} \sigma_{ij}, \quad \sigma_e = \sqrt{(3/2) s_{ij} s_{ij}}, \quad s_{ij} = \sigma_{ij} - \frac{1}{3} \sigma_{kk} \delta_{ij}$$

$$\phi = \frac{3}{2} \left(\frac{E}{E_s} - 1 \right).$$

When $\sigma_c < \sigma_T$

$$\phi = 0$$

E , ν , E_s and σ_T are the elastic modulus, Poisson coefficient, cutting modulus in unit tensile and yield stress, respectively.

The first variation of Π is

$$\delta \Pi = \int_v \left[\sigma_{ij} \delta s_{ij} + \left(s_{ij} - \frac{\partial V}{\partial \sigma_{ij}} \right) \delta \sigma_{ij} \right] dv - \int_{s_T} \bar{T}_i \delta u_i ds_T \quad (2)$$

where

$$\delta s_{ij} = \frac{1}{2} (\delta u_{i,j} + \delta u_{j,i}) + \frac{1}{2} (\delta u_{k,i} u_{k,j} + u_{k,i} \delta u_{k,j})$$

Using divergence theorem we can derive that

$$\begin{aligned} \delta \Pi = & - \int_v \{ \sigma_{ij,j} + (\sigma_{ijk} u_{k,i}), j \} \delta u_i dv \\ & + \int_v \left\{ s_{ij} - \left[\frac{1}{E} ((1+\nu) \sigma_{ij} - \nu \sigma_{kk} \delta_{ij}) + \frac{\phi}{E} s_{ij} \right] \right\} \delta \sigma_{ij} dv \\ & + \int_{s_T} \{ [\sigma_{ij} + (\sigma_{ijk} u_{k,i})] n_j - \bar{T}_i \} \delta u_i ds_T \\ & + \int_{s_n} \{ \sigma_{ij} + (\sigma_{ijk} u_{k,i}) \} n_j \delta u_i ds_n = 0 \end{aligned} \quad (3)$$

where n_j is the normal component of the reference coordinate prior to deformation on the boundary. It is not difficult to see that the Euler equations in (3) corresponds to the well known equilibrium equation, constitutive relation in deformation theory and boundary condition.

Equation (1) is similar to, but different from, those of Reissner's [4] in an elastic system. If we continue to proceed with a second order variation and notice that u_i and σ_{ij} are independent variables, $\delta^2 u_i = \delta^2 \sigma_{ij} = 0$. Based on these, we get

$$\delta^2 \Pi - Q = \int_v \left[\delta \sigma_{ij} \delta \epsilon_{ij} + \sigma_{ij} \delta^2 \epsilon_{ij} + \left(\delta \epsilon_{ij} - \frac{\partial^2 V}{\partial \sigma_{ij} \partial \sigma_{kl}} \delta \sigma_{kl} \right) \delta \sigma_{ij} \right] dv \quad (4)$$

where

$$\delta^2 \epsilon_{ij} = \delta u_{i,j} \delta u_{j,i}.$$

In the following, a new variation δ^* (refer to reference [8]) is made with respect to $\delta \sigma_{ij}$ and δu_i in the second order generalized function Q to obtain relevant equations and boundary conditions during buckling. Noticing the "consistent loading" condition, the stress, displacement and plastic modulus remain unchanged in the variation δ^* process. The "consistent loading" condition and its verification in general variation will be discussed in the following.

By using the divergence theorem, we can derive the following from equation (4):

$$\begin{aligned}
\delta^2 Q = & -2 \int_V \{ \delta \sigma_{ij,i} + (\delta \sigma_{ik} u_{i,k}), j + (\sigma_{ik} \delta u_{i,k}), j \} \delta^2 (u_i) dv \\
& + 2 \int_V \left\{ \delta \epsilon_{ij} - \left[\frac{1}{E} ((1+\nu) \delta \sigma_{ij} - \nu \delta \sigma_{kk} \delta_{ij}) \right. \right. \\
& \left. \left. + \frac{\delta \phi}{E} \delta_{ij} + \frac{\phi}{E} \delta s_{ij} \right] \right\} \delta^2 (\delta \sigma_{ij}) dv \\
& + 2 \int_S \{ \delta \sigma_{ij} + \delta \sigma_{ik} u_{i,k} + \sigma_{ik} \delta u_{i,k} \} n_j \delta^2 (u_i) ds = 0
\end{aligned} \quad (5)$$

where

$$\delta \phi = \frac{3}{2} \frac{\delta \sigma_i}{\sigma_i} \left(\frac{E}{E_i} - \frac{E}{E_p} \right), \quad \delta \sigma_i = \frac{3}{2} \frac{\epsilon_{ij} \delta s_{ij}}{\sigma_i}$$

E_t is the tangential modulus during unit tensile stress. The Euler equations in (5) correspond to the known equilibrium equation during buckling, incremental constitutive equation of deformation theory and boundary condition during buckling.

Substituting the relation between $\delta \epsilon_{ij}$, $\delta^2 \epsilon_{ij}$ and δu_i into equation (4) we can also get

$$\begin{aligned}
Q = & - \int_V \{ \delta \sigma_{ij,i} + (\delta \sigma_{ik} u_{i,k}), j + (\sigma_{ik} \delta u_{i,k}), j \} \delta u_i dv \\
& + \int_V \left\{ \delta \epsilon_{ij} - \left[\frac{1}{E} ((1+\nu) \delta \sigma_{ij} - \nu \delta \sigma_{kk} \delta_{ij}) \right. \right. \\
& \left. \left. + \frac{\delta \phi}{E} \delta_{ij} + \frac{\phi}{E} \delta s_{ij} \right] \right\} \delta \sigma_{ij} dv \\
& + \int_S \{ \delta \sigma_{ij} + \delta \sigma_{ik} u_{i,k} + \sigma_{ik} \delta u_{i,k} \} n_j \delta u_i ds
\end{aligned} \quad (6)$$

Comparing equation (6) to (5) we can see that Q and $\delta^* Q$ are similar in form.^[3,9] This is the same in the elastic case.

Therefore, when $\delta^* Q = 0$, $Q = 0$ and vice versa.

Thus, we proved that the first order variation of the generalized function Π in equation (1) can be used to derive various basic equations in the basic path to solve the problem

prior to buckling. By carrying out a new variation δ^* with respect to its second order variation can result in relevant equations during buckling.

II. Physical Significance of Generalized Functions Π and Q

Now, let us decompose the first term in the integral in equation (1)

$$\sigma_{ij}\epsilon_{ij} = \int_0^{\epsilon_{ij}} d(\sigma_{ij}\epsilon_{ij}) = \int_0^{\epsilon_{ij}} \epsilon_{ij} d\sigma_{ij} + \int_0^{\epsilon_{ij}} \sigma_{ij} d\epsilon_{ij} \quad (7)$$

where the function to be integrated ϵ_{ij} can be expressed in the form of stress and σ_{ij} can be expressed in the form of strain.

The second term of equation (1) is

$$V = \int_0^{\epsilon_{ij}} \frac{\partial V}{\partial \sigma_{ij}} d\sigma_{ij} \quad (8)$$

When $\epsilon_{ij} = \partial V / \partial \sigma_{ij}$ is valid, we get the following by substituting equation (7) into it

$$\sigma_{ij}\epsilon_{ij} = V = \int_0^{\epsilon_{ij}} \sigma_{ij} d\epsilon_{ij} \quad (9)$$

The right term represents the strain energy per unit volume.

Thus, Π in equation (1) is naturally equivalent to the definition of potential energy. For this reason, at the beginning of this paper we called it the generalized potential energy.

In order to determine stability, the classical definition /515 proposed by Dirichlet and Kelvin^[6] is that the body is in a state if the total amplitude of the added displacement caused by the deflection at any instance is arbitrarily small when the deflection itself is arbitrarily small. On the contrary, if an

arbitrarily small deflection would lead to a finite amplitude change, then it is unstable. Obviously, the necessary and sufficient condition is that the amount of internal energy stored or consumed when an infinitesimal displacement is added to the equilibrium position must be larger than the work done by an external force. In the 1930's, Trefftz^[7] and Kappus^[8] also applied this principle to derive the elastic buckling equation and stability determination criterion in the form of energy. In conjunction to the topic of this paper, for an arbitrarily small deflection $(\delta\sigma_{ij}, \delta u_i)$, if $\Delta\pi > 0$, it is stable, if $\Delta\pi < 0$, it is unstable.

From Taylor series expansion we know that

$$\begin{aligned} \Pi + \Delta\Pi = & \int_V [(\sigma_{ij} + \delta\sigma_{ij}) (e_{ij} + \delta e_{ij} + \frac{1}{2!} \delta^2 e_{ij}) \\ & - (V + \frac{\partial V}{\partial \sigma_{ij}} \delta\sigma_{ij} + \frac{1}{2!} \frac{\partial^2 V}{\partial \sigma_{ij} \partial \sigma_{kl}} \delta\sigma_{ij} \delta\sigma_{kl} \dots)] dV \\ & - \int_{\Gamma_T} \bar{T}_i (u_i + \delta u_i) d\Gamma \end{aligned}$$

Here, the external stress \bar{T}_i does not vary with deflection. Therefore, it is a case of "fixed load". By expanding the above equation, we get

$$\begin{aligned} \Pi + \Delta\Pi = & \left\{ \int_V [\sigma_{ij} e_{ij} - V] dV - \int_{\Gamma_T} \bar{T}_i u_i d\Gamma \right\} \\ & + \left\{ \int_V [\sigma_{ij} \delta e_{ij} + (e_{ij} - \frac{\partial V}{\partial \sigma_{ij}}) \delta\sigma_{ij}] dV - \int_{\Gamma_T} \bar{T}_i \delta u_i d\Gamma \right. \\ & + \left\{ \frac{1}{2!} \int_V \left[\delta\sigma_{ij} \delta e_{ij} + \sigma_{ij} \delta^2 e_{ij} + \left(\delta e_{ij} - \frac{\partial^2 V}{\partial \sigma_{ij} \partial \sigma_{kl}} \delta\sigma_{kl} \right) \delta\sigma_{ij} \right] dV \right. \\ & \left. \left. + \dots = \Pi + \delta\Pi + \frac{1}{2!} \delta^2\Pi \dots \right\} \right. \end{aligned} \quad (10)$$

Because $\delta\pi$ is already equal to zero, therefore, whether it is stable depends on $\delta^2\pi(=Q)$. If $Q>0$, it is stable. If $Q<0$, it is unstable. $Q=0$ is the stability limit. Above the stability limit or on buckling points, the criterion for stability is determined by higher order of variations of π , such as $\delta^3\pi$ This says that $Q=0$ may be stable or may be unstable. Therefore, $Q>0$ is only the sufficient criterion, but not the necessary criterion, for stability. After realizing the significance of $Q=0$ and knowing $Q=0$ corresponds to $\delta^*Q=0$, the reason why the buckling equation can be derived from $\delta^*Q=0$ is clear.

In addition, the following explanation is given to describe the relation between the condition $Q=0$ and the loss of uniqueness of the solution. If the uniqueness of the solution on the loading path is lost, then there must be other possible increments $\Delta\sigma_{ij}$ and Δu_i which satisfy:

$$\Delta\sigma_{ij,j} + (\Delta\sigma_{ik}u_{i,k}), j + (\sigma_{ik}\Delta u_{i,k}), j = 0 \quad (11)$$

$$\Delta\epsilon_{ij} = \frac{1}{E} [(1+\nu)\Delta\sigma_{ij} - \nu\Delta\sigma_{kk}\delta_{ij}] + \frac{\Delta\phi}{E}\epsilon_{ij} + \frac{\phi}{E}\Delta\epsilon_{ij} \quad (12)$$

$$\begin{aligned} \Delta T_i &= (\Delta\sigma_{ij} + \Delta\sigma_{ik}u_{i,k} + \sigma_{ik}\Delta u_{i,k})n_j = 0 && \text{on } s_T \\ \Delta u_i &= 0 && \text{on } s_u \end{aligned} \quad (13)$$

If we choose

$$\Delta\sigma_{ij} = \delta\sigma_{ij}, \Delta u_i = \delta u_i$$

We can see that the Euler equations in (11)-(13) are similar to those in (5). This means that the uniqueness of the solution is lost during buckling and vice versa. Therefore, the buckling point must be related to the loss of uniqueness of the solution. However, stability is not related to uniqueness, because buckling

is not equal to unstable.

In simplicity, buckling and loss of uniqueness of the solution correspond to $Q=0$ or $\delta^*Q=0$. Whether it is stable depends on $Q>0$ or $Q<0$. At $Q=0$, it depends on the sign of higher order variation terms in equation (10). /516

III. Investigation of "Consistent Loading" Condition

Hutchinson's^[2] argument can be extended to generalized variation in the following steps.

Under a "fixed load", the amplitude variation of the force (or displacement) load is proportional to a parameter. Its distribution is independent of this parameter. It was explained earlier that the necessary and sufficient condition for stability is $Q>0$. Now, let us re-write equation (4) into

$$Q = \int_V \left\{ 2\delta\sigma_{ij}(\delta u_{i,j} + u_{i,j}\delta u_{i,j}) + \sigma_{ij}\delta u_{i,j}\delta u_{i,j} - \left[\frac{1}{E} ((1+\nu)\delta\sigma_{ii} - \nu\delta\sigma_{kk}\delta_{ii}) + \alpha \left(\frac{\partial\phi}{\partial\sigma_{ii}}\delta\sigma_{ii} + \frac{\phi}{\sigma_{ii}}\delta\sigma_{ii} \right) \right] \delta\sigma_{ii} \right\} dV \quad (14)$$

where

$$\alpha = \begin{cases} 1 & \text{plastic loading} \\ 0 & \text{elastic loading} \\ 0 & \text{plastic loading followed by elastic unloading} \end{cases}$$

Let us take a solid body for comparison, i.e., an elastic comparative solid body. Its second order generalized function is defined as

$$Q_c = \text{right hand terms in (14), but } \alpha = \begin{cases} 1 & \text{plastic loading} \\ 0 & \text{elastic loading} \end{cases}$$

It is obvious that there is no elastic unloading zone in this case. To this end, an infinitesimal deflection $(\delta\sigma_{ij}, \delta u_i)$ is added to a known based state (σ_{ij}, u_i) . The difference between Q and Q_c is

$$Q = Q_c - I_c \quad (15)$$

where

$$I_c = \frac{1}{E} \int_{V_c} (\delta\phi_{,ii} + \phi_{,i}\delta s_{ii})\delta\sigma_{ii}dV_c \quad (16)$$

The subscript c represents the possible presence of an elastic unloading zone. By substituting the expressions for ϕ and $\delta\phi$ into (16) we get

$$I_c = \frac{1}{E} \int_{V_c} \left[\left(\frac{E}{E_c} - \frac{E}{E_c} \right) (\delta\sigma_{ii})^2 + \frac{3}{2} \left(\frac{E}{E_c} - 1 \right) \delta s_{ii} \delta s_{ii} \right] dV_c$$

because

$$\left(\frac{E}{E_c} - \frac{E}{E_c} \right) \geq 0, \quad \left(\frac{E}{E_c} - 1 \right) \geq 0$$

therefore $I_c \geq 0$, $Q \geq Q_c$.

This is to say that $Q=Q_c$ if a certain deflection is added to the entire body area V so that the plastic region remains plastic and elastic region remains elastic. Otherwise, $Q>Q_c$ if the additional deflection leads to the presence of an elastic unloading zone in V_c . Therefore, it is only necessary to find the corresponding characteristic function $(\delta\sigma_{ij}, \delta u_i)$ in Q_c in order to determine the minimum critical loading parameters because it is not possible to have even smaller critical loading parameters and other characteristic function distribution to make $Q=0$ while keeping $Q_c>0$. Thus, we proved that the "consistent loading" condition is still valid in the form of generalized

variation.

IV. Application in Analysis of Plate Shell Structure /517

In a thin wall plate shell, let us assume that the distributions of strain, stress, plane displacement and plastic parameter along the x_3 -direction are approximately:

$$\begin{aligned} & [\varepsilon_{\alpha\beta}, \sigma_{\alpha\beta}, \delta\varepsilon_{\alpha\beta}, \delta\sigma_{\alpha\beta}, u_{\alpha}, \phi] \\ & = [\varepsilon_{\alpha\beta}^{(0)}, N_{\alpha\beta}/h, \delta\varepsilon_{\alpha\beta}^{(0)}, \delta N_{\alpha\beta}/h, u_{\alpha}^{(0)}, \phi^{(0)}] \\ & + [K_{\alpha\beta}, 12M_{\alpha\beta}/h^3, \delta K_{\alpha\beta}, 12\delta M_{\alpha\beta}/h^3, w_{,\alpha}, 2\phi^{(0)}/h]x, \end{aligned} \quad (17)$$

where $\alpha, \beta=1$ or 2 and h is the wall thickness. By substituting the above into equation (1) and using the strain-stress relation in a plate shell^[9], we can get the following by integrating along x_3 and applying the divergence theorem:

$$\begin{aligned} \delta\Pi = & \int_{L_T} \left\{ [N_{\alpha\beta}] \delta u_{\alpha}^{(0)} \right. \\ & + [M_{\alpha\beta} + N_{\alpha\beta} b_{\alpha\beta} + N_{\alpha\beta} (w + w^{(i)})_{,\alpha\beta}] \delta w \\ & + \left[\varepsilon_{\alpha\beta}^{(0)} - \frac{1}{Eh} \left(C_{\alpha\beta\gamma\delta}^{(0)} N_{\gamma\delta} + \frac{2}{h} C_{\alpha\beta\gamma\delta}^{(0)} M_{\gamma\delta} \right) \right] \delta N_{\alpha\beta} \\ & + \left[K_{\alpha\beta} - \frac{12}{h^3} \left(\frac{h}{6} C_{\alpha\beta\gamma\delta}^{(0)} N_{\gamma\delta} + C_{\alpha\beta\gamma\delta}^{(0)} M_{\gamma\delta} \right) \right] \delta M_{\alpha\beta} \Big\} ds \\ & + \int_{L_T} [\dots] dL_T + \int_{L_n} [\dots] dL_n = 0 \end{aligned} \quad (18)$$

where $w^{(i)}$ is the initial deflection and $b_{\alpha\beta}$ is the curvature tensor

$$\left. \begin{aligned} C_{\alpha\beta\gamma\delta}^{(0)} &= (1+\nu) \left[\frac{1}{2} (\delta_{\alpha\gamma} \delta_{\beta\delta} + \delta_{\alpha\delta} \delta_{\beta\gamma}) - \frac{\nu}{1+\nu} \delta_{\alpha\beta} \delta_{\gamma\delta} \right] \\ &+ \phi^{(0)} \left[\frac{1}{2} (\delta_{\alpha\gamma} \delta_{\beta\delta} + \delta_{\alpha\delta} \delta_{\beta\gamma}) - \frac{1}{3} \delta_{\alpha\beta} \delta_{\gamma\delta} \right] \\ C_{\alpha\beta\gamma\delta}^{(1)} &= \phi^{(0)} \left[\frac{1}{2} (\delta_{\alpha\gamma} \delta_{\beta\delta} + \delta_{\alpha\delta} \delta_{\beta\gamma}) - \frac{1}{3} \delta_{\alpha\beta} \delta_{\gamma\delta} \right] \end{aligned} \right\} \quad (19)$$

Similar to the algorithm used in the first section, we apply a new variation δ^* to π for a second time. Then, we have

$$\begin{aligned} \delta^*(\delta^2 \Pi) - \delta^2 Q &= -2 \int_0^L \{ [\delta N_{\alpha\beta, \beta}] \delta^*(\delta u_{\alpha}^{(0)}) \\ &\quad + [\delta M_{\alpha\beta, \beta} + \delta N_{\alpha\beta} b_{\alpha\beta} + \delta N_{\alpha\beta} (w + w^{(1)})_{, \alpha\beta} \\ &\quad + N_{\alpha\beta} \delta w_{, \alpha\beta}] \delta^*(\delta w) \} ds \\ &\quad + 2 \int_0^L \left\{ \left[\delta u_{\alpha\beta}^{(0)} - \frac{1}{Eh} \left(D_{\alpha\beta\gamma\delta}^{(0)} \delta N_{\gamma\delta} + \frac{2}{h} D_{\alpha\beta\gamma\delta}^{(1)} \delta M_{\gamma\delta} \right) \right] \delta^*(\delta N_{\alpha\beta}) \right. \\ &\quad \left. + \left[\delta K_{\alpha\beta} - \frac{12}{Eh^3} \left(\frac{h}{6} D_{\alpha\beta\gamma\delta}^{(1)} \delta N_{\gamma\delta} + D_{\alpha\beta\gamma\delta}^{(0)} \delta M_{\gamma\delta} \right) \right] \delta^*(\delta M_{\alpha\beta}) \right\} ds \\ &\quad + \dots \end{aligned} \quad (20)$$

where

$$\left. \begin{aligned} D_{\alpha\beta\gamma\delta}^{(0)} &= (1 + \nu) \left[\frac{1}{2} (\delta_{\alpha\gamma} \delta_{\beta\delta} + \delta_{\alpha\delta} \delta_{\beta\gamma}) - \frac{\nu}{1 + \nu} \delta_{\alpha\beta} \delta_{\gamma\delta} \right] \\ &\quad + \phi_{\alpha\beta}^{(0)} \left[\frac{1}{2} (\delta_{\alpha\gamma} \delta_{\beta\delta} + \delta_{\alpha\delta} \delta_{\beta\gamma}) - \frac{1}{3} \delta_{\alpha\beta} \delta_{\gamma\delta} \right] + \phi_{\alpha\beta\gamma\delta}^{(0)} \\ D_{\alpha\beta\gamma\delta}^{(1)} &= \phi_{\alpha\beta}^{(1)} \left[\frac{1}{2} (\delta_{\alpha\gamma} \delta_{\beta\delta} + \delta_{\alpha\delta} \delta_{\beta\gamma}) - \frac{1}{3} \delta_{\alpha\beta} \delta_{\gamma\delta} \right] + \phi_{\alpha\beta\gamma\delta}^{(1)} \end{aligned} \right\} \quad (21)$$

/518

$$\begin{aligned} \phi_{\alpha\beta\gamma\delta} &= \frac{9}{4} \left(\frac{E}{E_1} - \frac{E}{E_2} \right) \zeta_{\alpha\beta\gamma\delta} \zeta_{\gamma\delta} - \phi_{\alpha\beta\gamma\delta}^{(0)} + \frac{2}{h} \phi_{\alpha\beta\gamma\delta}^{(1)} x_3 \\ \zeta_{\alpha\beta} &= \frac{1}{\sigma_1} \left[\frac{1}{2} (\delta_{\alpha\gamma} \delta_{\beta\delta} + \delta_{\alpha\delta} \delta_{\beta\gamma}) - \frac{1}{3} \delta_{\alpha\beta} \delta_{\gamma\delta} \right] \sigma_{\gamma\delta} \end{aligned}$$

From the above it is obvious that the third and fourth Euler equations in (18) and (20) correspond to the constitutive equations before and after buckling. From (19) and (21) we can see that the rigidity matrix correlating generalized strain to generalized stress is symmetric. However, when another method was used to derive it in reference [10] the favorable condition of matrix symmetry was not realized.

In the above, the plate shell belongs to the case of symmetric upper and lower cross-section relative to a neutral plane. For a non-symmetric cross-section with reinforcing ribs, an appropriately chosen generalized force can be used to simplify the equations.

Let us assume that there is a rib along the x-direction (neglecting twisting resistant rigidity). Its cross-sectional width is $b(z)$, i.e., it can vary along the z-direction. The stress and strain distribution on the cross-section are

$$\left. \begin{aligned} \sigma_x &= \left(\frac{N_x}{A_x} \right) + \left(\frac{M_x}{I_x} \right) z \\ \epsilon_x &= \epsilon_x^{(0)} + (K_x)z \end{aligned} \right\} \quad (22)$$

where A_x and I_x are the cross-sectional area and the moment of inertia relative to the neutral plane of the ribbed cross-section, respectively.

After substituting them into (1) and through certain operations we get

$$\begin{aligned} \delta \Pi = & - \int_x \left\{ \left[\frac{\partial}{\partial x} \left(N_x + J \frac{M_x}{I_x} \right) \right] \delta u \right. \\ & + \left[\frac{\partial^2}{\partial x^2} \left(I \frac{M_x}{I_x} + J \frac{N_x}{A_x} \right) + \left(N_x + J \frac{M_x}{I_x} \right) \frac{\partial^2 w}{\partial x^2} \right] \delta w \Big\} dx \\ & + \int_x \left\{ \epsilon_x^{(0)} H - \left[\frac{1}{E} \left(1 + \frac{2\phi^{(0)}}{3} \right) \left(N_x + J \frac{M_x}{I_x} \right) \right. \right. \\ & + \left. \left. \frac{2\phi^{(0)}}{3EH} \left(I \frac{M_x}{I_x} + J \frac{N_x}{A_x} \right) \right] \right\} \delta \left(\frac{N_x}{A_x} \right) dx \\ & + \int_x \left\{ K_x I - \left[\frac{1}{E} \left(1 + \frac{2\phi^{(0)}}{3} \right) \left(I \frac{M_x}{I_x} + J \frac{N_x}{A_x} \right) \right. \right. \\ & + \left. \left. \frac{2\phi^{(0)}}{3EH} \left(I \frac{N_x}{A_x} + G \frac{M_x}{I_x} \right) \right] \right\} \delta \left(\frac{M_x}{I_x} \right) dx + \dots \end{aligned} \quad (23)$$

where H is the height of the rib bar itself. Again, we have

$$A_s = \int b dx, J = \int b x dx, I = \int b x^2 dx, G = \int b x^3 dx$$

Let us assume that the spacing between the origin of the z coordinate and the neutral plane of the rib bar is e (usually the original can be chosen at the center plane of the plate shell), hence

$$J = A_s e, I = I_s + A_s e^2$$

From equation (23), in order to simplify the equation to the extent possible, especially in the equilibrium equation, we can define a new generalized force as:

$$N = N_s + J \frac{M_s}{I_s}, M = I \frac{M_s}{I_s} + J \frac{N_s}{A_s}$$

Thus, we can solve

$$N_s = \frac{IN - JM}{\left(I - \frac{J^2}{A_s}\right)}, M_s = I_s \frac{M - \frac{J}{A_s} N}{\left(I - \frac{J^2}{A_s}\right)}$$

Substituting back into (22), we get

/519

$$\sigma_s = \frac{1}{I - A_s e^2} \left[\left(\frac{I}{A_s} N - e M \right) + (M - e N) z \right] \quad (24)$$

Based on the above we know that although the relation between stress and generalized force is complicated by choosing N and M as the generalized forces (such as (24) in comparison to (22)), yet the equilibrium equation can be simplified.

V. Conclusions

The variational theorem introduced to analyze the structural plastic buckling based on deformation theory not only can be applied to mixed boundary problems but also provides a way to simplify the equations to be solved.

References

- [1] Hill, R., A general theory of uniqueness and stability in elastic/plastic solids, J. Mech. Phys. Solids, 6(1958), 236.
- [2] Hutchinson, J.W., Plastic buckling, Advances in Appl. Mech. (ed. by Chia-Shun Yih), 14 (1974), 67.
- [3] Bushnell, D., Bifurcation buckling of shells of revolution including large deflections, plasticity and creep, Int. J. Solids Structures, 10 (1974), 1287.
- [4] Reissner, E., On the Variational theorem in elasticity, J. Math. Phys., 29 (1950).
- [5] Li Guoshen, Wang Zifang and Han Jinhu, Elastic Buckling of Cylindrical Plate and Cylindrical Shell by Considering the Effect of Deformation before Buckling, ((Ribbed Cylindrical Plate and Cylindrical Shell)), (Shell and plate section of Solid Mechanics Research Laboratory, Institute of Mechanics, Academia Sinica), Chapter 4, Science Publishing Co. (1983).
- [6] Hill, R., On uniqueness and stability in the theory of finite elastic strain, J. Mech. Phys. Solids, 5 (1957), 229.
- [7] Trefftz, E., Zur theorie der stabilitat des elastischen gleichgewichts, Zeit. fur Angew. Math. u Mech. B13 (1933), 160.

- [8] Kappus, R., Zur elastizitats theorie endlicher verschiebungen, Zeit. fur Angew. Math. u Mech. B19 (1939), 344.
- [9] A.C. Woolmill, Flexible Plate and Flexible Shell (translated by Lu Wenda et al), Science Publishing Co. (1963).
- [10] Li Guochen, Axial Creep Buckling of Cylindrical Shell, Journal of Mechanics, 1(1981) 38.

A GENERAL VARIATIONAL THEOREM FOR THE STRUCTURAL PLASTIC BUCKLING ANALYSIS USING THE DEFORMATION THEORY

Li Guochen

(Institute of Mechanics, Academia Sinica)

Abstract

Following the form given by Reissner in 1950 for elastic analysis, a general variational functional in plasticity is prescribed as Π in eq. (1). By setting its first variation $\delta\Pi$ due to the variation of (σ_{ij}, u_i) to zero, the Euler equations derived in (3) are proved to be the equilibrium equations, a deformation type of stress-strain relations and boundary conditions for the prebuckling fundamental path solution. As Kappus had done in 1939, a new variation δ^* can be imposed on $(\delta\sigma_{ij}, \delta u_i)$. Let $Q = \delta^2\Pi$, then from δ^*Q of eq. (5), the basic incremental equations are derived for the evaluation of critical loading and its corresponding buckling pattern. Comparing (5) and (6) it can be seen that whenever δ^*Q equals zero the same is Q or vice versa.

From eqs. (7)–(9) it is shown that eq. (1) is essentially equivalent to the potential energy. According to the definition of Dirichlet and Kelvin, stability depends on whether $\Delta\Pi$ is positive or negative. Using the Taylor series expansion eq. (10) brings out that (a) if $Q > 0$, stable (b) if $Q < 0$, unstable (c) when $Q = 0$, buckling occurs, it is the limit of stability, the stability at this point relies on the sign of the higher variation term, e. g. $\delta^3\Pi \dots$. On the other hand, when the uniqueness of the solution fails, then the possible incremental parts $(\Delta\sigma_{ij}$ and $\Delta u_i)$ should satisfy eqs. (11)–(13), which are similar to the Euler equations in (5).

A comparison solid which has no unloading condition within the plastic region at the moment of buckling is introduced to solve the buckling problem. Application of the above theorem in the plate and shell problems is exemplified.

END

FILMED

1-86

DTIC